Physica D 440 (2022) 133440

Contents lists available at ScienceDirect

Physica D

journal homepage: www.elsevier.com/locate/physd

Review

Nonlinear optical waveguide lattices: Asymptotic analysis, solitons, and topological insulators

Mark J. Ablowitz [a], Justin T. Cole [b,*]

[a] Department of Applied Mathematics, University of Colorado, Campus Box 526, Boulder, CO, USA
[b] Department of Mathematics, University of Colorado, Colorado Springs, CO, USA

ARTICLE INFO

Article history:
Received 17 January 2022
Received in revised form 4 July 2022
Accepted 5 July 2022
Available online 11 July 2022
Communicated by Dmitry Pelinovsky

Keywords:
Photonics
Waveguide arrays
Tight-binding approximations
Solitons
Topological insulators

ABSTRACT

In recent years, there has been considerable interest in the study of wave propagation in nonlinear photonic lattices. The interplay between nonlinearity and periodicity has led researchers to manipulate light and discover new and interesting phenomena such as new classes of localized modes, usually referred to as solitons, and novel surface states that propagate robustly. A field where both nonlinearity and periodicity arises naturally is nonlinear optics. But there are other areas where waves propagating on background lattices play an important role, including photonic crystal fibers and Bose–Einstein condensation. In this review article the propagation of wave envelopes in one and two-dimensional periodic lattices associated with additional potential in the nonlinear Schrödinger (NLS) equation, termed lattice NLS equations, are studied. A discrete reduction, known as the tight-binding approximation, is employed to find the linear dispersion relation and the equations governing nonlinear discrete envelopes for two-dimensional simple periodic lattices and two-dimensional non-simple honeycomb lattices. In the limit under which the envelopes vary slowly, continuous envelope equations are derived from the discrete system. The coefficients of the linear evolution system are related to the dispersion relation in both the discrete and continuous cases. For simple lattices, the continuous systems are NLS type equations. In honeycomb lattices, in certain cases, the continuous system is found to be nonlinear Dirac equations. Finally, it is possible to realize so-called topological insulator systems in an optical waveguide setting. The modes supported by these systems are associated with spectral topological invariants and, remarkably, can propagate without backscatter from lattice defects.

Contents

* Corresponding author.
E-mail addresses: mark.ablowitz@colorado.edu (M.J. Ablowitz), jcole13@uccs.edu (J.T. Cole).

https://doi.org/10.1016/j.physd.2022.133440
0167-2789/

1. Introduction

In nonlinear optics, periodic structures that have been carefully studied are arrays of coupled nonlinear optical waveguides. These waveguides typically consist of media with higher refractive indices that tend to confine and steer light beams. The first theoretical prediction of discrete solitons in an optical waveguide array was reported by Christodoulides and Joseph [1]. Many properties of such discrete solitons were subsequently studied cf. [2,3]. However, after the theoretical prediction of [1], it was almost a decade until self-trapping of light in nonlinear waveguide array was experimentally observed [4].

Early on, it was difficult to fabricate specialized materials with fixed geometry at such small scales. This has been largely overcome by optical and etching techniques. A schematic illustrating the coupled waveguide configuration used in [4] is given in Fig. 1. The array consists of approximately 40 waveguide "ridges" that are 4 μm wide and 0.95 μm deep; the longitudinal propagation length of the waveguide is 6 mm. An input laser beam is injected at the central location of the waveguides. The results of the experiment are shown in Fig. 2. At low power, the beam diffracts; at moderate power, the beam begins to self-focus. Finally, at high power the beam strongly self-focuses and a highly localized soliton beam is observed.

A few years later, a new method of creating optical periodic lattices in photosensitive materials using optical induction was proposed [5]. Soon afterwards, using this 'all optical' technique two-dimensional (2D) periodic lattices were created and 2D solitons were observed and studied [6,7]. These solitons are sometimes termed 'gap' solitons because they are found in the frequency gaps of the underlying periodic wave spectrum. This area has attracted considerable interest from engineers, physicists, and mathematicians. Subsequently, many novel types of localized modes, e.g. solitons, have been predicted theoretically and demonstrated experimentally. Examples include dipole solitons [8], vortex solitons [9], soliton trains [10], etc.

The experimental results of [7] are depicted in Fig. 3. Here, as with the one dimensional configuration, at low input power the beam diffracts and at high input power the beam self-focuses and a localized structure is seen to emerge; i.e., a soliton is formed.

Researchers usually model the above phenomena by a general 2D lattice nonlinear Schrödinger (NLS) equation, written in dimensionless form:

$$i\psi_z + \nabla^2\psi - V(\mathbf{r})\psi + f(|\psi|^2)\psi = 0,$$

where $\nabla^2 = \partial_x^2 + \partial_y^2$, $\mathbf{r} = (x, y)$ is the transverse spatial dimensions, and z (the direction of propagation) behaves like a temporal variable. The effective refractive index is split into two parts: a linear periodic potential $V(\mathbf{r})$, and an intensity-dependent nonlinear term $f(|\psi|^2)$. The most commonly studied type of nonlinearity is cubic, i.e. $f(|\psi|^2) = \sigma|\psi|^2$ where σ is constant. This model describes light propagation in a periodic Kerr nonlinear medium as well as in Bose–Einstein condensates trapped in a 2D optical lattice [11]. A representation of a typical cross-section of two-dimensional rectangular lattice potential, $V(x, y)$, is given in Fig. 4. Here the maxima and minima play the role of the 'ridges and valleys' in the waveguide (high and low refractive index).

We note that the photonic material employed in experiments [6,7] used so-called photorefractive media, not Kerr media; in this case, the nonlinearity/potential is usually modeled by saturable nonlinear media

$$-V(\mathbf{r}) + f(|\psi|^2) \to -(1 - W(\mathbf{r}) + \sigma|\psi|^2)^{-1}.$$

Despite their different forms, saturable nonlinearity reduces to a cubic/Kerr nonlinearity in the small refractive index limit, $|W(\mathbf{r}) + \sigma|\psi|^2| \ll 1$, where

$$-(1 - W(\mathbf{r}) + \sigma|\psi|^2)^{-1} \approx (-1 - W(\mathbf{r}) + \sigma|\psi|^2)$$

and $V(\mathbf{r}) = -1 - W(\mathbf{r})$. In [5,12], this type of saturable lattice was used numerically and shown to yield solitons at high input power.

After these results in 2D periodic lattices were reported, many novel localized structures were predicted theoretically and demonstrated experimentally. Examples include dipole solitons, vortex solitons, soliton trains, cf. [8–10,13,14]. Similarly, in condensed matter physics, ultracold atoms, Bose–Einstein condensates (BECs) can be trapped in a periodic optical lattice which is described by a lattice NL equation, also known as the Gross–Pitaevskii equation. The experimental observation of gap solitons in BECs was reported in [15], and vortices theoretically predicted in [16]. With observations and theory in different fields, the study of related phenomena such as localized modes and their properties has gained significant scientific interest.

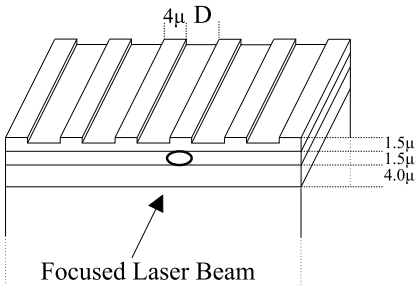

Fig. 1. Schematic illustrating the coupled waveguide array used in [4]. Reprinted figure with permission from [4], copyright (1998) by the American Physical Society.

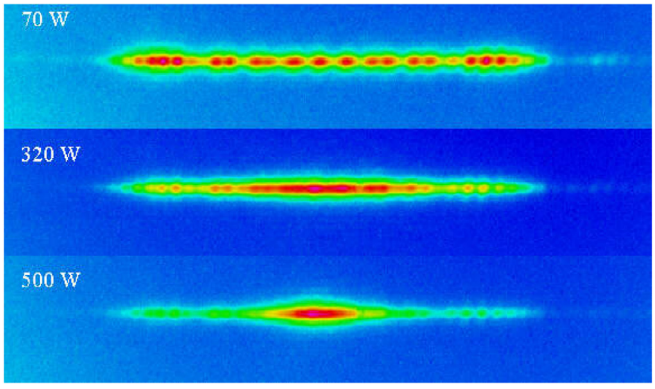

Fig. 2. Output field measured at the output facet of the waveguide. Input power: (top) low, (middle) medium, and (bottom) high. A solitary wave forms at high power. Reprinted figure with permission from [4], copyright (1998) by the American Physical Society.

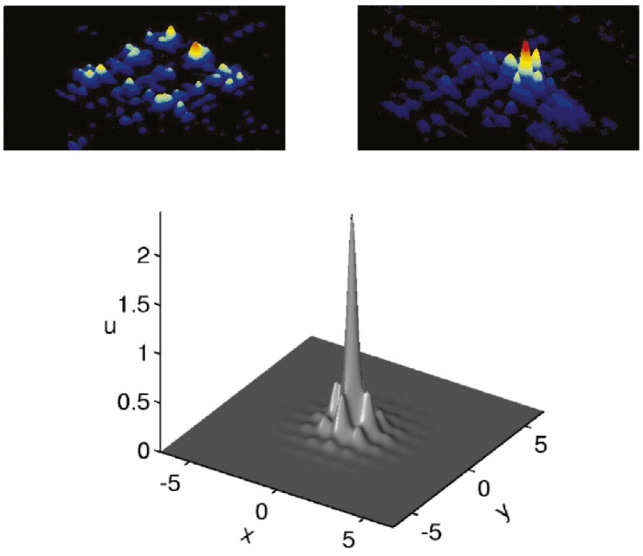

Fig. 3. (Top) Output intensity measurements obtained in a nonlinear waveguide array. Left, low input power; Right, high input power. Reprinted by permission from Springer Nature: Nature [7], copyright (2003). (Bottom) Numerically obtained lattice soliton at high power. Reprinted figure with permission from [12], copyright (2003) by the American Physical Society.

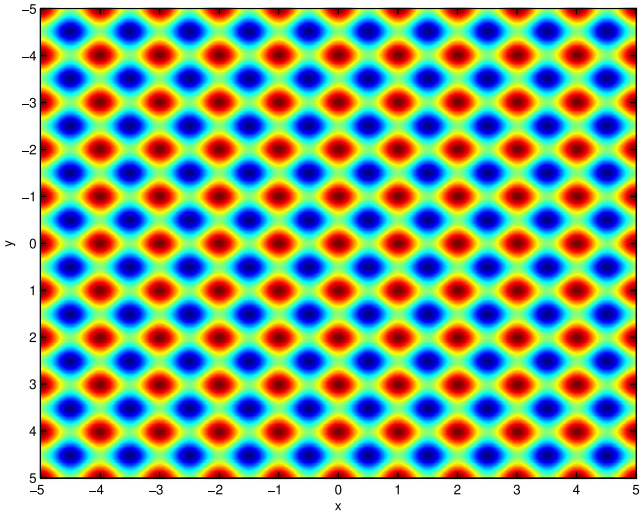

Fig. 4. $V(x, y) = V_0(\cos^2 \pi x + \cos^2 \pi y)$; $V_0 = 1$.

Background lattice periodicity alone leads to interesting mathematical investigations. An important feature follows from what it is often termed Bloch theory [17]. Namely, the associated spectrum has multi-band structure. Bands are regions that support bounded, quasi-periodic, eigenmodes. Between two adjacent bands, there can exist a gap where bounded linear eigenmodes do not exist. Analogous to Fourier modes, Bloch modes can propagate in a periodic linear waveguide; here different Bloch modes admit different dynamics that, in turn, do not influence each other because of the superposition principle.

Nonlinearity can change the eigenmodes associated with band structures. The spectral regions where modes propagate can be extended by nonlinearity into the band gaps. So, in the gap region where linear bounded modes do not propagate, i.e. are forbidden, there can exist nonlinear bounded eigenmodes. Localized nonlinear gap modes are known as *band gap solitons*. The dynamics can become more interesting with nonlinearities; for example, in BECs, nonlinear Bloch oscillations, nonlinear Landau–Zenner tunneling etc. have been reported; cf. [15]. In optics, conical diffraction that was thought to be a linear phenomena is also exhibited in nonlinear honeycomb lattices [18]. In addition, since the superposition principle does not hold when nonlinearity is present, different Bloch modes may interfere each other. Energy can spread among these linear Bloch modes and new Bloch modes may be produced due to interference—as seen in supercontinuum generation [19,20]. Asymptotic descriptions can be obtained via multiple-scales approach, as in [21–24].

The geometric distribution of local minima of the potentials, also called *sites*, can be used to classify the potentials. These sites are the positions of the potential wells. In optics, they have increased refractive index and the electromagnetic field is attracted to these regions. The distribution of these sites greatly influence the properties of the associated dynamics/waves. Discrete one dimensional evolution equations on 1D lattices were studied by the so-called Wannier function approach in (cf. [2,25]). However, there are significant differences that occur among 2D periodic lattices.

First, we will divide 2D periodic lattices into two groups: simple and non-simple stationary (z-independent) lattices. Simple lattices only have one site in a basic unit cell while non-simple lattices have more than one site per cell. Examples of simple lattices are rectangular and triangular lattices. A well-known non-simple lattice is the honeycomb hexagonal lattice that has two sites in a unit cell and breaks up into two triangular sublattices. Due to the underlying symmetries in the honeycomb lattice, we will see below that the dispersion relation of the associated Bloch theory may have isolated degenerate points where two dispersion surfaces touch each other. These are called Dirac points and near these points the dispersion surface has a conical structure. It was rigorously proven in [26] that dispersion surfaces touch each other at Dirac points.

The evolution of a Bloch mode envelope in the neighborhood of these points is governed by nonlinear Dirac systems [18]. There are interesting phenomena associated with the Dirac system. An example in optics is conical diffraction—where a narrow beam transforms into bright expanding rings, see [18,27,28]. Honeycomb lattices also admit various types of band gap solitons that like other 2D periodic lattices is due to the effect of nonlinearity; cf [29]. Another important application is the material graphene that has a honeycomb lattice structure, see [30]. In BECs, honeycomb background lattices may also lead to interesting phenomena, see [31].

From the field of beam propagation in waveguide arrays, naturally came a way to realize a type of system (or media) known as a *topological insulator* (TI) in a photonic setting. Topological insulators have their origins in condensed matter physics, and in particular the quantum Hall effect [32–34]. The first discussion of a TI in an electromagnetic system can be traced back to the seminal work of Haldane and Raghu [35]. The experimental realization of a TI in an electromagnetic system with anisotropic permeability; i.e. in a magneto-optic system occurred soon afterwards [36]. The realization of a TI in a photonic system came a few years later [37] and notably did not require an external magnetic field. Instead, researchers induced an *effective* magnetic field by fabricating waveguides that helically-varied in the direction of beam propagation. These studies assumed the wave propagation was linear. Interest in the field of topological insulators in electromagnetic systems has expanded considerably since this earlier research—see e.g. [38,39].

In a topological insulator system, linear wave propagation is possible at frequencies lying in band gaps of the spectrum, typically when they propagate along the boundary or surface of the lattice media; these are called edge modes. Wave propagation

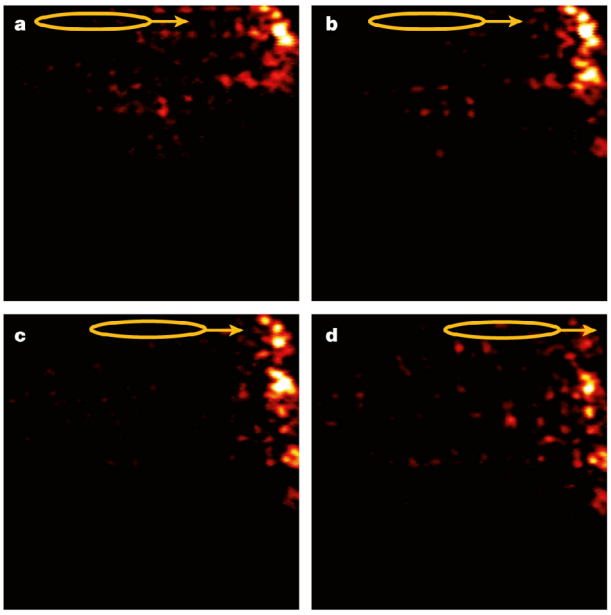

Fig. 5. Experimental results from a Floquet topological insulator in a helically-driven waveguide array. (a–d) Yellow ellipses shows input beam location, output beam is shown in heat map. Collectively, the snapshots show a unidirectional edge mode which does not backscatter at corners Reprinted by permission from Springer Nature: Nature [37], copyright (2013).

in the interior of the media (well away from any boundaries) is still prohibited at these frequencies; these are known as bulk modes. To induce this behavior, one type of system referred to as *Floquet systems*, are generated by driving the lattice potential and creating equations with coefficients that are periodic in z. The associated linear eigenmodes possess so-called *topological invariants* which through a principle known as the bulk-edge correspondence, indicate the presence of *topologically protected* edge states which propagate unidirectionally. These modes are localized along the domain boundary and are exceptionally robust to defects in the lattice system; they do not suffer from backscatter and only move forward (See Fig. 5). Furthermore, weak nonlinearity induces *edge solitons* see [40–42]. These solitons inherit the topological properties of their linear counterpart, yet also manage to balance dispersion and nonlinearity, like a typical soliton. Several linear and nonlinear results are discussed in this review. Another notable TI system is the Su–Schrieffer–Heeger (SSH) model. It occurs in non-driven waveguide lattices where the coupling strength among adjacent sites alternates.

Before outlining the content of this article, we note this review does not include a thorough discussion of parity-time (PT) symmetric systems. Since their theoretical proposal in the photonic systems in 2008 [43,44], this class of systems has been heavily studied. Indeed, stable PT-symmetric modes were experimentally realized in a waveguide array [45,46]. We omit details of this subfield, which is extensive, in order to focus on the basics of optical waveguides and topological insulators systems.

Another important realization of waveguide arrays that we do not consider in detail is that of planar lattices governed by the linearly polarized 2D Maxwell's equations. For non-magnetized systems, the governing PDE for time-harmonic solutions is the variable-coefficient Helmholtz equation [47]. The variable coefficient is due to the permittivity function that models the dielectric of the waveguides. These systems can exhibit similar properties to those found in Schrödinger operators (mentioned below) which possess Dirac points in honeycomb lattices [48,49] and localized edge states [50]. Moreover, these systems also extend to topological insulators. Indeed, the seminal works of [35,36,51] showed the existence of in-plane TE and TM topologically protected modes, respectively.

Now we outline the topics covered in this review. The general methodology of the tight-binding approximation is discussed in Section 2. In Section 3 the equations governing the tight-binding equations and envelope dynamics of a class of simple lattices are derived. As an example, a simple square lattice is considered in Section 4. The two-dimensional harmonic oscillator and its relationship to the orbital approximation are shown in Section 5. Next, tight-binding models for non-simple lattices is described in Section 6.

From here, the realization of topological insulators in optical waveguides is explored in Section 7. The well-known one dimensional SSH model is relatively simple to realize in an optical waveguide setting; it is described in Section 8. In Section 9 a class of longitudinally driven, Floquet-type 2D lattices are shown to support unidirectional edge mode propagation with associated Chern invariants. We conclude in Section 10.

2. Fundamentals

The analysis here follows closely that in [18,52,53]. We will consider the 2D lattice nonlinear Schrödinger (NLS) equation with cubic nonlinearity, written in dimensionless form:

$$i\psi_z + \nabla^2\psi - V(\mathbf{r})\psi + \sigma|\psi|^2\psi = 0, \tag{2.1}$$

where $\mathbf{r} = (x, y)$, z is a temporal variable, $V(\mathbf{r})$ is the periodic potential and σ is a constant that is positive for focusing nonlinearity and negative for defocusing nonlinearity. This model can be used to describe paraxial light propagation in a periodic Kerr nonlinear medium [54,55] and Bose–Einstein condensates trapped in a 2D optical lattice [11].

The potential $V(\mathbf{r})$ is a 2D periodic, bounded, and real-valued function with two primitive lattice vectors, $\mathbf{v}_1$ and $\mathbf{v}_2$. The potential has the translational symmetry $V(\mathbf{r} + m\mathbf{v}_1 + n\mathbf{v}_2) = V(\mathbf{r})$, for any $m, n \in \mathbb{Z}$. We denote $\mathbb{P} = \{m\mathbf{v}_1 + n\mathbf{v}_2 : m, n \in \mathbb{Z}\}$ as the set of lattice vectors and $\mathbf{k}_1$ and $\mathbf{k}_2$ as the primitive reciprocal lattice vectors and $\mathbb{G} = \{m\mathbf{k}_1 + n\mathbf{k}_2 : m, n \in \mathbb{Z}\}$ as the set of reciprocal lattice vectors. The unit cell of the physical lattice, denoted by Ω, is the parallelogram with $\mathbf{v}_1$ and $\mathbf{v}_2$ as its two sides and the unit cell of the reciprocal lattice, Ω', is the parallelogram determined by $\mathbf{k}_1$ and $\mathbf{k}_2$. The relationship between lattice and reciprocal lattice is $\mathbf{v}_m \cdot \mathbf{k}_n = 2\pi\delta_{mn}$.

We first consider a simple periodic lattice that has one local minimum site per unit cell. With a starting point and the lattice vectors, all the positions of the sites can be constructed. All sites form a discrete lattice in the $\mathbf{r}$ plane, namely $\mathbb{P}$. We use $S_\mathbf{v}$ to denote the position of the site with index $\mathbf{v}$ and $S_\mathbf{v} = S_\mathbf{0} + \mathbf{v}$ where $S_\mathbf{0}$ is the starting point of the site lattice, i.e, $S_\mathbf{0} \in \Omega$. Due to translational symmetry, one unit cell has all the information of periodic functions. For simplicity, we place $S_\mathbf{0} = \mathbf{0}$ and choose the parallelogram determined by $\mathbf{v}_1$ and $\mathbf{v}_2$ whose center is $S_\mathbf{0}$ as the primitive unit cell Ω. We also choose the parallelogram determined by $\mathbf{k}_1$ and $\mathbf{k}_2$ whose center is $\mathbf{k} = \mathbf{0}$ as the primitive reciprocal unit cell Ω'. On the other hand, a non-simple lattice may have more than one site in one unit cell. One may need more than one starting point to construct the lattice. An example of a non-simple lattice is a honeycomb lattice. These two situations are illustrated in Fig. 6. For the square lattice, all sites are 'black' and they can be constructed by integer translations of the two primitive vectors. On the other hand, the honeycomb lattice consists of 'black' and 'white' sites. The black and white sites are separately constructed from the underlying primitive vectors.

Let us first consider solutions of Eq. (2.1) when the nonlinear coefficient σ is negligibly small, or equivalently $|\psi|^2 \ll 1$, so that

$$i\psi_z + \nabla^2\psi - V(\mathbf{r})\psi = 0. \tag{2.2}$$

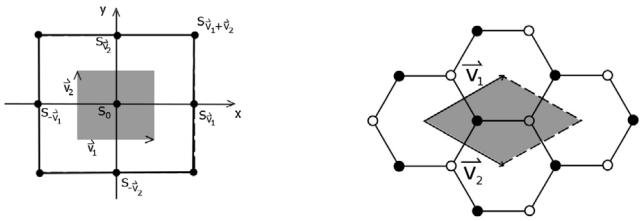

Fig. 6. (Left) A typical simple lattice. (Right) A non-simple honeycomb lattice. In each case the lattice sites (corresponding to minima of potential $V(\mathbf{r})$) are denoted by dots. The shaded region is a fundamental cell.

Special separable solutions, which form a complete set, take the form $\psi(\mathbf{r}, z) = \varphi(\mathbf{r})e^{-i\mu z}$ and then Eq. (2.2) transforms to the following eigenvalue problem

$$\nabla^2\varphi - V(\mathbf{r})\varphi = -\mu\varphi. \tag{2.3}$$

According to Bloch theory (cf. [17]), the eigenfunction, also called a Bloch mode or Bloch wave, has the $\mathbf{k}$-dependent form

$$\varphi(\mathbf{r};\mathbf{k}) = e^{i\mathbf{k}\cdot\mathbf{r}}u(\mathbf{r};\mathbf{k}),$$

where $u(\mathbf{r};\mathbf{k})$ has the same periodicity as the potential $V(\mathbf{r})$ for any $\mathbf{k}$. Physically, $\mathbf{k}$ is known as quasi-momentum. It is convenient to introduce the following two operators:

$$\mathcal{H} \equiv \nabla^2 - V(\mathbf{r}), \qquad \mathcal{H}_{\mathbf{k}} \equiv \nabla^2 + 2i\mathbf{k}\cdot\nabla - |\mathbf{k}|^2 - V(\mathbf{r}),$$

where $\mathcal{H}$ is the Schrödinger operator with a periodic potential and $\mathcal{H}_{\mathbf{k}}$ is a $\mathbf{k}$-dependent operator, defined on $L^2(\Omega)$; hence $u(\mathbf{r};\mathbf{k})$ satisfies the following eigenvalue problem,

$$\mathcal{H}_{\mathbf{k}}u(\mathbf{r};\mathbf{k}) = -\mu u(\mathbf{r};\mathbf{k}); \quad u(\mathbf{r}+\mathbf{v}_s;\mathbf{k}) = u(\mathbf{r};\mathbf{k}); \quad s = 1, 2,$$

where $\mu = \mu(\mathbf{k})$ is called the dispersion relation. On the other hand, Bloch mode $\varphi(\mathbf{r};\mathbf{k})$ satisfies the eigenproblem with quasi-periodic boundary condition

$$\mathcal{H}\varphi(\mathbf{r};\mathbf{k}) = -\mu\varphi(\mathbf{r};\mathbf{k}); \varphi(\mathbf{r}+\mathbf{v}_s;\mathbf{k}) = e^{i\mathbf{k}\cdot\mathbf{v}_s}\varphi(\mathbf{r};\mathbf{k}) \tag{2.4}$$

for $s = 1, 2$. Note that after one period the Bloch mode comes back to its original value, up to a phase factor.

Assume that $\mu(\mathbf{k}) = \mu(\mathbf{k}+\mathbf{g})$ for any $\mathbf{g} \in \mathbb{G}$. We also note that $\varphi(\mathbf{r};\mathbf{k})$ and $\varphi(\mathbf{r};\mathbf{k}+\mathbf{g})$ satisfy the same eigenvalue problem and boundary condition Eq. (2.4) due to $\mathbf{v}\cdot\mathbf{g} = 2\pi m$ for any $\mathbf{v} \in \mathbb{P}$ and $\mathbf{g} \in \mathbb{G}$. So for any $\mathbf{r}$, $\varphi(\mathbf{r};\mathbf{k})$ is periodic with respect to $\mathbf{k}$, thus $\mathbf{k}$ is restricted in the parallelogram determined by $\mathbf{k}_1$ and $\mathbf{k}_2$.

It is noted that for an arbitrary value of $\mathbf{k}$, the Bloch mode $\varphi(\mathbf{r};\mathbf{k})$ is usually not a periodic function of $\mathbf{r}$. However, there are some special values of $\mathbf{k}$, where $\varphi(\mathbf{r};\mathbf{k})$ is periodic or anti-periodic with two periods $\mathbf{v}_1$ and $\mathbf{v}_2$. For example, At the Γ point ($\mathbf{k} = \mathbf{0}$) that is located at the center of the Brillouin zone, $\varphi(\mathbf{r};\mathbf{0})$ is periodic (see boundary condition in Eq. (2.4)). At the X_s, $s = 1, 2$ points ($\mathbf{k} = \frac{1}{2}\mathbf{k}_s, s = 1, 2$), which are located at the middle of one side of the Brillouin parallelogram, we have: $\varphi(\mathbf{r}+\mathbf{v}_s;\frac{1}{2}\mathbf{k}_s) = -\varphi(\mathbf{r};\frac{1}{2}\mathbf{k}_s)$ and $\varphi(\mathbf{r}+\mathbf{v}_{3-s};\frac{1}{2}\mathbf{k}_s) = \varphi(\mathbf{r};\frac{1}{2}\mathbf{k}_s)$. At the M point ($\mathbf{k} = \frac{1}{2}\mathbf{k}_1 + \frac{1}{2}\mathbf{k}_2$) that is located at one vertex of the Brillouin parallelogram, we have: $\varphi(\mathbf{r}+\mathbf{v}_1;\frac{1}{2}\mathbf{k}_1+\frac{1}{2}\mathbf{k}_2) = -\varphi(\mathbf{r};\frac{1}{2}\mathbf{k}_1+\frac{1}{2}\mathbf{k}_2)$ and $\varphi(\mathbf{r}+\mathbf{v}_2;\frac{1}{2}\mathbf{k}_1+\frac{1}{2}\mathbf{k}_2) = -\varphi(\mathbf{r};\frac{1}{2}\mathbf{k}_1+\frac{1}{2}\mathbf{k}_2)$; See Fig. 7 below. Thus at the Γ, X_s and M points, which are special locations in the reciprocal lattice fundamental cell, the corresponding Bloch modes are either periodic or anti-periodic. In addition, at these special points the Bloch modes can be made real since the multiplicative factor in Eq. (2.4) is real and consequently, the eigenfunctions can also be taken to be real.

For each $\mathbf{k}$, the operator $\mathcal{H}_{\mathbf{k}}$ has an infinite set of discrete eigenvalues $\mu(\mathbf{k}) = \mu_j(\mathbf{k}), j = 0, 1, 2, \ldots$. Thus, the dispersion

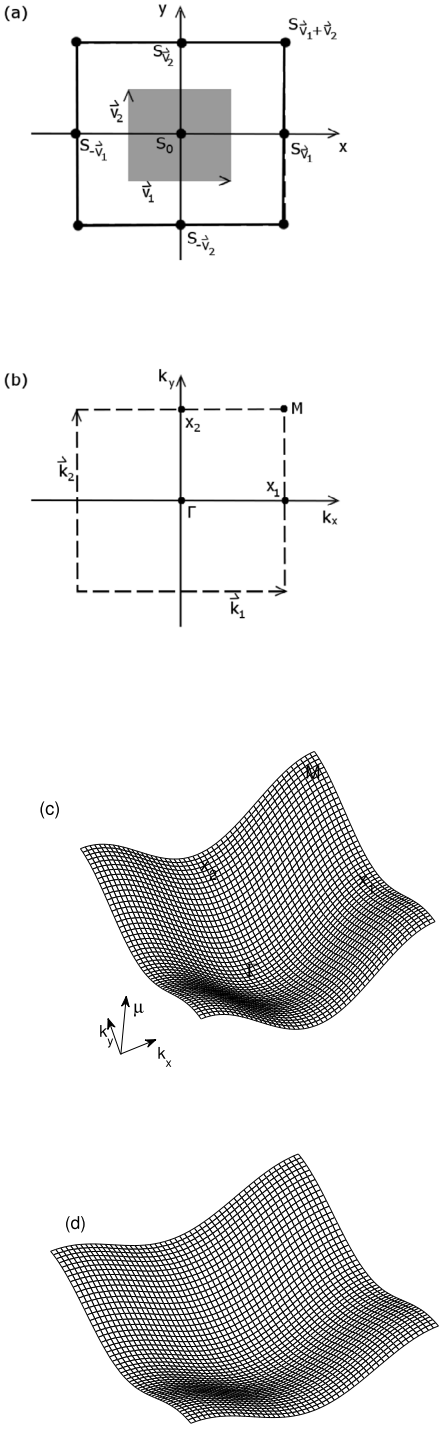

Fig. 7. (a) The site distributions of the square lattice Eq. (4.1). The shadow region is the primitive unit cell. (b) The Brillouin zone of the square lattice—the square surrounded by the dashed lines. The first dispersion relation band (c) obtained from direction simulation and (d) from the approximate formula (4.2). Reprinted by permission from Wiley: Studies in Applied Math. [53], copyright (2012).

relation μ, its corresponding eigenfunctions and the associated Bloch modes could have an additional subscript j to indicate different eigenvalues. Here, for simplicity, we will usually omit the subscript j. Hence the spectrum of the Schrödinger operator $\mathcal{H}$ has multiple band structures and therefore may exhibit band gaps between two dispersion surfaces, where bounded Bloch modes are not allowed. As $\mathbf{k}$ varies, the discrete eigenvalue $\mu(\mathbf{k})$ and the corresponding eigenfunctions $u(\mathbf{r};\mathbf{k})$ as functions of $\mathbf{k}$

are assumed to be smooth over $\mathbf{k}$. Later on, it will no longer necessarily be the case that the eigenfunctions are smooth in $\mathbf{k}$. Chern insulators contain eigenmodes with discontinuous phase topology [56].

Since $\varphi(\mathbf{r};\mathbf{k})$ is periodic in $\mathbf{k}$, we can represent it as a Fourier series

$$\varphi(\mathbf{r};\mathbf{k}) = \sum_{\mathbf{v}\in\mathbb{P}} \phi_{\mathbf{v}}(\mathbf{r}) e^{i\mathbf{k}\cdot\mathbf{v}} \tag{2.5}$$

where the Fourier coefficient $\phi_{\mathbf{v}}(\mathbf{r})$ is defined as

$$\phi_{\mathbf{v}}(\mathbf{r}) = \frac{1}{|\Omega'|}\int_{\Omega'} \varphi(\mathbf{r};\mathbf{k}) e^{-i\mathbf{k}\cdot\mathbf{v}} d\mathbf{k} \tag{2.6}$$

and is the so-called Wannier function [57]. From here on, the sum over $\mathbf{v}$ means $\mathbf{v}$ takes all values in $\mathbb{P}$, i.e., $\mathbf{v} = m\mathbf{v}_1 + n\mathbf{v}_2$, for all $m, n \in \mathbb{Z}$.

From definition Eq. (2.6), we can see that

$$\begin{aligned}\phi_{\mathbf{v}}(\mathbf{r}) &= \frac{1}{|\Omega'|}\int_{\Omega'} \varphi(\mathbf{r};\mathbf{k}) e^{-i\mathbf{k}\cdot\mathbf{v}} d\mathbf{k}\\ &= \frac{1}{|\Omega'|}\int_{\Omega'} u(\mathbf{r};\mathbf{k}) e^{i\mathbf{k}\cdot(\mathbf{r}-\mathbf{v})} d\mathbf{k}\\ &= \frac{1}{|\Omega'|}\int_{\Omega'} \varphi(\mathbf{r}-\mathbf{v};\mathbf{k}) d\mathbf{k} = \phi_{\mathbf{0}}(\mathbf{r}-\mathbf{v})\end{aligned}$$

due to the periodic nature of $u(\mathbf{r};\mathbf{k})$. This equation shows that all Wannier modes are merely translations of the primitive Wannier mode, $\phi_{\mathbf{0}}(\mathbf{r})$. Usually, the subscript $\mathbf{0}$ is omitted and the Wannier function is referred to as $\phi(\mathbf{r}-\mathbf{v})$. Wannier functions have all the information of the Bloch modes, yet they do not depend on $\mathbf{k}$. If one has all Wannier function coefficients, then the exact Bloch mode can be constructed through (2.5), or vice versa via Eq. (2.6). In general, is not possible to compute either Bloch modes or Wannier functions explicitly. However, under some limits, such as tight-binding/deep lattice limit (i.e., $|V(\mathbf{r})| \gg 1$), they can be constructed by asymptotic analysis that in turn provides crucial analytical understanding. Details will be discussed below.

For a periodic potential, the local minima are called the sites. Physically, local minima are the positions of potential wells and in optics correspond to increased refractive index to which the electric field is attracted. In the tight-binding limit, the potential well at each site is very deep, hence it often turns out that the Wannier function defined in Eq. (2.6) is localized at the site $S_{\mathbf{v}}$, becoming more localized as the depth increases. Physically speaking, Bloch modes tend to concentrate most of their energy in the neighborhood of these sites. The lattice sites are waveguides that effectively trap the wave function with some weak coupling among nearby lattice sites.

The potential function describing the periodic lattice can be written in the form

$$V(\mathbf{r}) = \sum_{\mathbf{v}} V_s(\mathbf{r}-\mathbf{v}). \tag{2.7}$$

where $V_s(\mathbf{r})$ denotes the potential well at the site $S_{\mathbf{0}}$. It originally is defined only in the cell Ω (i.e., its support is only the primitive unit cell Ω). We also define

$$\Delta V(\mathbf{r}) = V(\mathbf{r}) - V_s(\mathbf{r}).$$

Moreover, we will extend the domain of $V_s(\mathbf{r})$ to the whole plane with fast decaying tails. Since the overall value of the potential is not important, here we take the potential to satisfy $\max_{\mathbf{r}}\{V(\mathbf{r})\} = 0$. For an arbitrary potential that does not satisfy this requirement, we can just simply subtract its maximum value through a phase transformation of $\psi(\mathbf{r}, z)$. Mathematically, a way to construct a periodic function is to let $V_s(\mathbf{r})$ be a rapidly decaying function and then repeat this function under translational shifts of the lattice vectors. A periodic function is now a sum of rapidly decaying functions that are the same up to a spatial shift. In the tight-binding limit: $V_s(\mathbf{r})$ of a simple periodic potential can be approximated by $V(\mathbf{r}) \approx -V_0 e^{-k_0^2(x^2+y^2)}$ with $k_0^2 \gg 1$. We note that if the potential has more than one local minima in a unit cell, i.e., a non-simple lattice, then we apply this approximation near each distinct site type.

3. Simple lattices, nonlinear envelope dynamics

3.1. Dispersion relations

In order to understand the envelope dynamics in weakly nonlinear periodic media, we need a good understanding of the associated linear problem. The linear problem is governed by a linear Schrödinger equation with a periodic potential and the dispersion relation, $\mu(\mathbf{k})$, plays a key role.

Since $\mu(\mathbf{k})$ is a periodic function of $\mathbf{k}$, it can be represented in a Fourier series

$$\mu(\mathbf{k}) = \hat{\mu}_{\mathbf{0}} + \sum_{\mathbf{v}\neq\mathbf{0}} \hat{\mu}_{\mathbf{v}} e^{i\mathbf{k}\cdot\mathbf{v}}. \tag{3.1}$$

where $\hat{\mu}_{\mathbf{v}} = \hat{\mu}^*_{-\mathbf{v}}$ since $\mu(\mathbf{k})$ is real. For a simple 2D periodic potential we will estimate the order of $\hat{\mu}_{\mathbf{v}}$ and find the leading order contributions. The 1D lattice is a special case. For a 1D lattice, it turns out that $\mu(k) \approx \hat{\mu}_0 + 2\hat{\mu}_1\cos(kl)$ with $|\hat{\mu}_1| \gg |\hat{\mu}_n|$, $n > 1$ where l is the 1D period.

In the tight-binding limit, we assume the Wannier functions Eq. (2.6) are localized at the lattice sites and decay exponentially. This allows us to use WKB expansions where the harmonic oscillator is a good approximation. To leading order, the Wannier function can be approximated by "orbitals", defined as

$$\left[\nabla^2 - V_s(\mathbf{r})\right]\phi(\mathbf{r}) = -E\phi(\mathbf{r}), \tag{3.2}$$

where E is the real discrete eigenvalue of the operator $\nabla^2 - V_s(\mathbf{r})$, also called orbital energy. In other words, Wannier functions defined in Eq. (2.6) satisfy the eigenvalue problem Eq. (3.2) to leading order. We do not distinguish between orbitals and Wannier functions here. For convenience, we require that the orbitals are real and have norm 1, i.e., $\int \phi^2(\mathbf{r})d\mathbf{r} = 1$. We define

$$\mathcal{H}^{\mathbf{v}} \equiv \nabla^2 - V_s(\mathbf{r}-\mathbf{v})$$

where $\mathcal{H}^{\mathbf{v}}$ is a self-adjoint operator defined in $L^2(\mathbb{R}^2)$. So, E and $\phi(\mathbf{r}-\mathbf{v})$ are the eigenvalue and corresponding eigenfunction of $\mathcal{H}^{\mathbf{v}}$. Moreover, $\mathcal{H}^{\mathbf{v}}$ usually has a infinite number of discrete eigenvalues if $V_s(\mathbf{r})$ is bounded. In this chapter, we will discuss the lowest band, where using orbitals to construct the Bloch mode is reasonable if $V_s(\mathbf{r})$ is deep: $|V_s| \gg 1$.

Next, we use a discrete approach to compute the dispersion relation. Substituting the Bloch mode Eq. (2.5) into the eigenvalue problem (2.3), we get

$$[\mathcal{H}^{\mathbf{0}} + E]\varphi(\mathbf{r}) = [E - \mu + \Delta V(\mathbf{r})]\varphi(\mathbf{r}).$$

For the ground state, we assume the nullspace of the operator $\mathcal{H}^{\mathbf{0}} + E$ is one dimensional. Then the Fredholm condition associated with $\mathcal{H}^{\mathbf{0}}$ gives

$$\int \phi(\mathbf{r})\left[(E-\mu) + \Delta V(\mathbf{r})\right]\varphi(\mathbf{r})d\mathbf{r} = 0.$$

Substituting the decomposition of the Bloch mode Eq. (2.5) into the above condition yields the dispersion relation

$$\mu = E + \frac{\sum_{\mathbf{v}} \lambda_{\mathbf{v}} e^{i\mathbf{k}\cdot\mathbf{v}}}{\sum_{\mathbf{v}} \kappa_{\mathbf{v}} e^{i\mathbf{k}\cdot\mathbf{v}}}, \tag{3.3}$$

where

$$\lambda_{\mathbf{v}} = \int \phi(\mathbf{r})\Delta V(\mathbf{r})\phi(\mathbf{r}-\mathbf{v})d\mathbf{r}$$

$$\kappa_{\mathbf{v}} = \int \phi(\mathbf{r})\phi(\mathbf{r}-\mathbf{v})d\mathbf{r} = \kappa_{-\mathbf{v}}.$$

The dispersion relation in Eq. (3.3) can be simplified. Note that $\kappa_{\mathbf{0}} = 1$ and $\lambda_{\mathbf{v}} \ll 1$ and $\kappa_{\mathbf{v}} \ll 1$ when $\mathbf{v} \neq \mathbf{0}$ because $\phi(\mathbf{r})$ is localized. To leading order, the dispersion relation is: $\mu \sim E + \lambda_{\mathbf{0}} \sim \hat{\mu}_{\mathbf{0}}$; i.e., the mean value of μ. Since $\sum_{\mathbf{v}\neq\mathbf{0}} \kappa_{\mathbf{v}} e^{i\mathbf{k}\cdot\mathbf{v}} \ll 1$, we have

$$\mu \approx E + \lambda_{\mathbf{0}} + \sum_{\mathbf{v}\neq\mathbf{0}} C_{\mathbf{v}} e^{i\mathbf{k}\cdot\mathbf{v}} \tag{3.4}$$

where

$$C_{\mathbf{v}} = \lambda_{\mathbf{v}} - \lambda_{\mathbf{0}}\kappa_{\mathbf{v}}.$$

Comparing Eqs. (3.1) and (3.4), we see $\hat{\mu}_{\mathbf{v}} \approx C_{\mathbf{v}}$, for $\mathbf{v} \neq \mathbf{0}$. Hence, we have calculated the first few Fourier coefficients of the dispersion relation $\mu = \mu(\mathbf{k})$.

Furthermore, we need only take the leading order terms of $\sum_{\mathbf{v}} C_{\mathbf{v}} e^{i\mathbf{k}\cdot\mathbf{v}}$. Note that both $\lambda_{\mathbf{v}}$ and $\kappa_{\mathbf{v}}$ decay fast as $|\mathbf{v}| \to \infty$. So we only need to consider the nearest neighbor and on-site interactions for the dominant contributions. This is the tight-binding approximation that has been widely used in solid state physics to calculate electronic band structure (cf. [58]). Then we get the dispersion relation

$$\mu(\mathbf{k}) = E + \lambda_{\mathbf{0}} + \sum_{\langle\mathbf{v}\rangle} C_{\mathbf{v}} e^{i\mathbf{k}\cdot\mathbf{v}}. \tag{3.5}$$

Here and afterwards $\langle\mathbf{v}\rangle$ indicates the sum over $\mathbf{v}$ only takes nearest (nonzero) neighbor shift vectors. For convenience, we also define

$$\omega(\mathbf{k}) = \sum_{\langle\mathbf{v}\rangle} C_{\mathbf{v}} e^{i\mathbf{k}\cdot\mathbf{v}}.$$

It is noted that $E + \lambda_{\mathbf{0}}$ has no $\mathbf{k}$ dependence and only determines the mean value of the frequency. The $\mathbf{k}$ dependence of the dispersion relation is determined by $\omega(\mathbf{k})$. When considering nearest neighbor interactions, we typically assume that $C_{\mathbf{v}}$ for all nearest neighbor shift vectors have the same values and denote

$$C = C_{\mathbf{v}_1}.$$

So, for any nearest neighbor shift vector $\mathbf{v}$, $C_{\mathbf{v}} \sim O(C)$. In the tight-binding limit, C is very small. So $\omega(\mathbf{k})$ is order $O(C)$. It is also seen that as $V_0 \to \infty$, $C \to 0$ and consequently $\omega(\mathbf{k}) \to 0$. Hence the dispersion surface in Eq. (3.5) becomes flatter and flatter. On the other hand, the two nearest orbital energy difference $E_{j+1} - E_j \sim O(\sqrt{V_0})$, so $E_{j+1} - E_j \to \infty$. Consequently, there may exist a gap between $\mu_{j+1}(\mathbf{k})$ and $\mu_j(\mathbf{k})$.

Note that the ground state (lowest eigenfunction) of the operator $\mathcal{H}^{\mathbf{v}}$ is taken to be simple; however, the eigenvalues associated with the higher excited states can be degenerate; i.e., there can be multiple eigenfunctions corresponding to one eigenvalue. The interested reader can find a discussion of the higher states in [53].

3.2. Envelope dynamics

Similar to Fourier modes, the Bloch modes form a complete set in the space of L^2 functions [59,60]. As a result, an L^2 function can be decomposed into Bloch mode components [23,24].

In the linear limit, the dynamics of Bloch modes are determined by the dispersion relation. Due to the superposition principle of linear problems, different Bloch modes have different dynamics and they do not mix with each other. However, when nonlinearity is present, the dynamics is more subtle. Although the derivation of the equation for a continuous envelope in space–time is well-known, it is not obvious how one can derive the equations for a discrete, in space, envelope.

When $\mu(\mathbf{k})$ has a single dispersion relation branch, we assume to leading order

$$\psi(\mathbf{r}, z, Z) \sim \sum_{\mathbf{v}} a_{\mathbf{v}}(Z)\phi(\mathbf{r}-\mathbf{v})e^{i[\mathbf{k}\cdot\mathbf{v}-\mu(\mathbf{k})z]}. \tag{3.6}$$

Here $a_{\mathbf{v}}$ represents the Bloch wave mode envelope at the site $S_{\mathbf{v}}$. We assume the envelope $a_{\mathbf{v}}(Z)$ varies slowly under evolution, where $Z = \varepsilon z$ for a small parameter ε that will be determined later.

Substituting the envelope representation Eq. (3.6) into the lattice NLS Eq. (2.1), one obtains

$$\begin{aligned}
&\left(\mathcal{H}^{\mathbf{p}} + E\right)\left(\sum_{\mathbf{v}} a_{\mathbf{v}}(Z)\phi(\mathbf{r}-\mathbf{v})e^{i\mathbf{k}\cdot\mathbf{v}}\right) \\
&\quad = -\sum_{\mathbf{v}}\left(\varepsilon i\frac{da_{\mathbf{v}}}{dZ} + a_{\mathbf{v}}\left[\mu - E - \Delta V(\mathbf{r}-\mathbf{p})\right]\right)\phi(\mathbf{r}-\mathbf{v})e^{i\mathbf{k}\cdot\mathbf{v}} \\
&\qquad - \sigma\left(\sum_{\mathbf{v}} a_{\mathbf{v}}\phi(\mathbf{r}-\mathbf{v})e^{i\mathbf{k}\cdot\mathbf{v}}\right)^2\left(\sum_{\mathbf{v}} a_{\mathbf{v}}\phi(\mathbf{r}-\mathbf{v})e^{i\mathbf{k}\cdot\mathbf{v}}\right)^*,
\end{aligned} \tag{3.7}$$

where $\mathbf{p} \in \mathbb{P}$. The Fredholm condition associated with $\mathcal{H}^{\mathbf{p}}$, i.e., $\int F\phi(\mathbf{r}-\mathbf{p}) = 0$ where F represents the right hand side (RHS) of Eq. (3.7), yields

$$\begin{aligned}
&\sum_{\mathbf{v}'} i\varepsilon\kappa_{\mathbf{v}'}\frac{da_{\mathbf{p}+\mathbf{v}'}}{dZ}e^{i\mathbf{k}\cdot\mathbf{v}'} + \sum_{\mathbf{v}'} a_{\mathbf{p}+\mathbf{v}'}\left[(\mu - E)\kappa_{\mathbf{v}'} - \lambda_{\mathbf{v}'}\right]e^{i\mathbf{k}\cdot\mathbf{v}'} \\
&+ \sigma\sum_{\mathbf{v}_1}\sum_{\mathbf{v}_2}\sum_{\mathbf{v}_3}\gamma_{\mathbf{v}_1\mathbf{v}_2\mathbf{v}_3}a_{\mathbf{v}_1}a_{\mathbf{v}_2}a^*_{\mathbf{v}_3} = 0,
\end{aligned}$$

where $\mathbf{v} = \mathbf{p} + \mathbf{v}'$ and only leading order terms are considered and

$$\begin{aligned}
&\gamma_{\mathbf{v}_1\mathbf{v}_2\mathbf{v}_3} = e^{i\mathbf{k}\cdot(\mathbf{v}_1+\mathbf{v}_2-\mathbf{v}_3)}\times \\
&\int \phi(\mathbf{r}-\mathbf{p}-\mathbf{v}_1)\phi(\mathbf{r}-\mathbf{p}-\mathbf{v}_2)\phi(\mathbf{r}-\mathbf{p}-\mathbf{v}_3)\phi(\mathbf{r}-\mathbf{p})d\mathbf{r}.
\end{aligned}$$

When only on-site and nearest neighbor interactions are taken into account, the governing equation, after dropping the prime notation, is

$$i\varepsilon\frac{da_{\mathbf{p}}}{dZ} + \omega(\mathbf{k})a_{\mathbf{p}} - \sum_{\langle\mathbf{v}\rangle} a_{\mathbf{p}+\mathbf{v}}C_{\mathbf{v}}e^{i\mathbf{k}\cdot\mathbf{v}} + g\sigma|a_{\mathbf{p}}|^2a_{\mathbf{p}} = 0, \tag{3.8}$$

where $g = \gamma_{\mathbf{000}} = \int \phi(\mathbf{r})^4 d\mathbf{r}$ is the only on-site interaction term taken for the nonlinear term. Here we assume that ε, σ and C all have the same order to ensure maximal balance.

After rescaling, we obtain the nonlinear discrete evolution equation

$$i\frac{da_{\mathbf{p}}}{dZ} + \widetilde{\omega}(\mathbf{k})a_{\mathbf{p}} - \sum_{\langle\mathbf{v}\rangle} a_{\mathbf{p}+\mathbf{v}}\widetilde{C}_{\mathbf{v}}e^{i\mathbf{k}\cdot\mathbf{v}} + gs(\sigma)|a_{\mathbf{p}}|^2a_{\mathbf{p}} = 0, \tag{3.9}$$

where for convenience we have taken $\varepsilon = |C| = |\sigma|$; $\widetilde{\omega} = \frac{\omega}{|C|}$; $\widetilde{C}_{\mathbf{v}} = \frac{C_{\mathbf{v}}}{|C|}$ and $s(\sigma)$ is the sign of σ. Eq. (3.9) is the unified discrete nonlinear wave system that describes the dynamics of a single envelope in any simple nonlinear periodic lattice. Note that the linear coefficients of the equation are directly related to the coefficients of the linear dispersion relation in the tight-binding limit, defined in Eq. (3.5). We also note that the 1D reduction is obtained as a special case; i.e., either the vector $\mathbf{v}$ is one dimensional or the 2D lattice is well-approximated by a

1D lattice. So if $\mathbf{v_1} = l\hat{\mathbf{i}}$ and we omit $\mathbf{v_2}$, the 1D lattice equation is given in 1D notation by

$$i\frac{da_p}{dZ} + \widetilde{\omega}(k)a_p - (a_{p+l}\widetilde{C}_{p+l}e^{ikl} + a_{p-l}\widetilde{C}_{p-l}e^{-ikl}) + gs(\sigma)|a_p|^2 a_p = 0. \tag{3.10}$$

The derivation of the tight-binding models above can be made rigorous. In particular, it is possible to show that the Wannier expansion (2.5) approaches the solution of the lattice NLS Eq. (2.1) in the deep-lattice limit, i.e. $V_0, |V_s| \to \infty$, using an appropriate Sobolev norm. The works of [61–64] have proven this for various lattice Schrödinger equations with different types of deep, but periodic potentials.

3.3. Continuum reduction

Next, we consider the continuous limit. Assume that the envelope $a_{\mathbf{v}}$ varies slowly over $\mathbf{v}$. In other words, the envelope takes the form

$$\psi(\mathbf{r}, Z) \sim \sum_{\mathbf{v}} a_{\mathbf{v}}(Z)\phi(\mathbf{r}-\mathbf{v})e^{i\mathbf{k}\cdot\mathbf{v}}e^{-i\mu z} \approx \sum_{\mathbf{v}} a(\mathbf{R}, Z)\phi(\mathbf{r}-\mathbf{v})e^{i\mathbf{k}\cdot\mathbf{v}}e^{-i\mu z}$$

where $\mathbf{R} = (X, Y) = \nu\mathbf{r}$ now denotes the coordinate of the envelope and $\nu \ll 1$. To leading order, $a_{\mathbf{v}} \approx \int a(\mathbf{R})\phi^2(\mathbf{r}-\mathbf{v})d\mathbf{r} \approx a(\nu(\mathbf{R}-S_{\mathbf{v}}))$ where $a_{\mathbf{v}}$ is defined at site points.

Before proceeding, we recall our assumption that the dispersion relation is sufficiently smooth at the $\mathbf{k}$ value we are studying. We also introduce some further notation: $\partial_m \equiv \frac{\partial}{\partial \mathbf{r}_m}$ and $\nabla \equiv (\partial_1, \partial_2)^T$; $\widetilde{\partial}_m \equiv \frac{\partial}{\partial \mathbf{R}_m}$ and $\widetilde{\nabla} \equiv (\widetilde{\partial}_1, \widetilde{\partial}_2)^T$; $\overline{\partial}_m \equiv \frac{\partial}{\partial \mathbf{k}_m}$ and $\overline{\nabla} \equiv (\overline{\partial}_1, \overline{\partial}_2)^T$; $\partial_{m,n} \equiv \partial_m\partial_n$. Here $m = 1$ denotes the x-direction and $m = 2$ is the y-direction.

Using Taylor expansion, we get

$$a_{\mathbf{p}+\mathbf{v}} \approx a_{\mathbf{p}} + \nu\mathbf{v}\cdot\widetilde{\nabla}a_{\mathbf{p}} + \frac{\nu^2}{2}\mathbf{v}\mathbf{H}\mathbf{v}^T a_{\mathbf{p}},$$

where $\mathbf{H} = \begin{pmatrix} \widetilde{\partial}_{11} & \widetilde{\partial}_{12} \\ \widetilde{\partial}_{21} & \widetilde{\partial}_{22} \end{pmatrix}$ is the Hessian matrix operator.

Then

$$\sum_{\langle\mathbf{v}\rangle} a_{\mathbf{p}+\mathbf{v}}C_{\mathbf{v}}e^{i\mathbf{k}\cdot\mathbf{v}} \approx$$

$$a_{\mathbf{p}}\sum_{\langle\mathbf{v}\rangle} C_{\mathbf{v}}e^{i\mathbf{k}\cdot\mathbf{v}} + \nu\widetilde{\nabla}a_{\mathbf{p}}\cdot\sum_{\langle\mathbf{v}\rangle}\mathbf{v}C_{\mathbf{v}}e^{i\mathbf{k}\cdot\mathbf{v}} + \frac{\nu^2}{2}\sum_{\langle\mathbf{v}\rangle} C_{\mathbf{v}}e^{i\mathbf{k}\cdot\mathbf{v}}\mathbf{v}\mathbf{H}\mathbf{v}^T a_{\mathbf{p}}$$

$$= a_{\mathbf{p}}\omega(\mathbf{k}) - i\nu\overline{\nabla}\mu\cdot\widetilde{\nabla}a_{\mathbf{p}} - \frac{\nu^2}{2}\sum_{m,n=1}^{2}\overline{\partial}_{m,n}\mu\widetilde{\partial}_{m,n}a_{\mathbf{p}}. \tag{3.11}$$

Substituting Eq. (3.11) into Eq. (3.8) yields, to leading order, the equation

$$i\varepsilon\frac{\partial a}{\partial Z} + i\nu\overline{\nabla}\mu\cdot\widetilde{\nabla}a + \frac{\nu^2}{2}\sum_{m,n=1}^{2}\overline{\partial}_{m,n}\mu\widetilde{\partial}_{m,n}a + g\sigma|a|^2 a = 0,$$

where $a \equiv a_p$ is a continuous function now. The above equation, whose coefficients depend on $\mu(\mathbf{k})$, governs the dynamics of a single Bloch mode envelope in nonlinear simple periodic media. It is valid for any value of $\mathbf{k}$. In analogy to homogeneous media, $\overline{\nabla}\mu$ plays the role of the group velocity; it is the velocity of the envelope. In special cases, $\overline{\nabla}\mu = \mathbf{0}$. This condition gives the extrema of the dispersion surface, and at these points, the group velocity is zero and the envelope will remain at its initial position. The envelope has a spatial shift in the cross-section when propagating along z direction if $\overline{\nabla}\mu \neq \mathbf{0}$. However, by defining a moving frame variable $\boldsymbol{\xi} = \mathbf{R} - \overline{\nabla}\mu Z$ we find the equation

$$i\frac{da}{dZ} + \frac{1}{2}\sum_{m,n=1}^{2}\overline{\partial}_{m,n}\widetilde{\mu}\,\widetilde{\partial}_{m,n}a + s(\sigma)|a|^2 a = 0, \tag{3.12}$$

where $\widetilde{\mu} = \frac{\mu}{|C|}$ and $s(\sigma)$ is the sign of σ and the matrix $\overline{\partial}_{m,n}\widetilde{\mu}$ is typically called the Hessian. Here we have taken the maximal balance condition $\varepsilon \sim O(\nu^2|C|) \sim O(g|\sigma|)$. The above Eq. (3.12) is a 2D nonlinear Schrödinger equation. At different values of $\mathbf{k}$, the linear dispersive terms may be elliptic, hyperbolic or even parabolic.

4. A typical simple lattice—square lattice

In the previous section, we derived the dispersion relation for arbitrary simple lattices and the dynamics of Bloch mode envelopes. In this section, we will use a typical square lattice to apply the above general analysis. For convenience, we assume the nonlinearity is focusing, i.e., $\sigma > 0$. Square 2D periodic structures are common in nature and can be readily engineered in optics (cf. [7] and Fig. 4).

A typical square lattice is

$$V(x, y) = \frac{V_0}{2}(\sin^2(k_0 x) + \sin^2(k_0 y) - 2), \tag{4.1}$$

where $0 \geq V(\mathbf{r}) \geq -V_0$, $V_0 > 0$ is the lattice intensity and k_0 is the scaled wavelength of the interfering plane waves. The characteristic vectors are

$$\mathbf{v}_1 = l\,(1, 0)\,, \qquad \mathbf{v}_2 = l\,(0, 1)\,,$$
$$\mathbf{k}_1 = \frac{2\pi}{l}\,(1, 0)\,, \qquad \mathbf{k}_2 = \frac{2\pi}{l}\,(0, 1)\,,$$

where $l = \frac{\pi}{k_0}$ is the lattice constant. Clearly, $\mathbf{v}_i\cdot\mathbf{k}_j = 2\pi\delta_{ij}$ and the potential has periodicity $V(x + ml, y + nl) = V(x, y)$ for $m, n \in \mathbb{Z}$.

The site distribution is displayed in Fig. 7(a). For this potential, each site has four nearest neighbors. Note that $S_{\mathbf{v}_1+\mathbf{v}_2}$ is not one of the nearest neighbors of $S_{\mathbf{0}}$. The nearest shift vectors are $\mathbf{v}_1$, $-\mathbf{v}_1$, $\mathbf{v}_2$, $-\mathbf{v}_2$.

For the first band, we find that

$$C_{\mathbf{v}_1} = C_{\mathbf{v}_2} = C \approx -0.056V_0\exp\left(-\frac{\sqrt{V_0}\,\pi^2}{4\sqrt{2}k_0}\right) < 0$$

(see below for further details). So the dispersion relation of the first band is

$$\mu(\mathbf{k}) = E + \lambda_{\mathbf{0}} + 2C\left[\cos(\mathbf{k}\cdot\mathbf{v}_1) + \cos(\mathbf{k}\cdot\mathbf{v}_2)\right], = E + \lambda_{\mathbf{0}} + 2C\left[\cos(lk_x) + \cos(lk_y)\right]. \tag{4.2}$$

The Brillouin zone that is also a square is displayed in Fig. 7(b), as well as special points. The dispersion relation obtained by direct numerical simulation of the eigenproblem (2.4) is displayed in Fig. 7(c) and it agrees both qualitatively and quantitatively very well with the dispersion relation obtained by the formula (4.2), shown in Fig. 7(d).

From the analytical formula Eq. (4.2), we readily obtain

$$\overline{\mathbf{H}}\mu = -2l^2C\begin{pmatrix} \cos(lk_x) & 0 \\ 0 & \cos(lk_y) \end{pmatrix}. \tag{4.3}$$

Here $\overline{\mathbf{H}} = \begin{pmatrix} \overline{\partial}_{11} & \overline{\partial}_{12} \\ \overline{\partial}_{21} & \overline{\partial}_{22} \end{pmatrix}$ is the Hessian matrix operator with respect to $\mathbf{k}$.

Next we describe the dispersive nature of the system at special symmetry points. At the Γ point, the Hessian matrix is

$$\overline{\mathbf{H}}\mu = -2l^2C\begin{pmatrix} 1 & 0 \\ 0 & 1 \end{pmatrix}.$$

So Γ is a minimum point. Furthermore, since $C < 0$ the governing equation of the envelope is a focusing NLS equation. It is expected that band gap solitons will bifurcate from this point, see [65].

At the M point, the Hessian matrix is

$$\overline{\mathbf{H}}\mu = -2l^2C\begin{pmatrix} -1 & 0 \\ 0 & -1 \end{pmatrix}.$$

So M is a maximum point since $-C > 0$. The governing equation of the envelope is a defocusing NLS equation. There may exist dark solitons.

At the X_1 point, the Hessian matrix is

$$\overline{\mathbf{H}}\mu = -2l^2C\begin{pmatrix} -1 & 0 \\ 0 & 1 \end{pmatrix}.$$

So X_1 is a saddle point. The governing equation is a hyperbolic focusing NLS equation. We note that this version of NLS describes deep water waves [66].

At the X_2 point, the Hessian matrix is

$$\overline{\mathbf{H}}\mu = -2l^2C\begin{pmatrix} 1 & 0 \\ 0 & -1 \end{pmatrix}.$$

So X_2 is also a saddle point but with opposite negative and positive eigen-directions to X_1.

5. 2D quantum harmonic oscillator

In this section, we discuss the case when $V(\mathbf{r})$ is large and is locally harmonic at each site, i.e., for $V_0 \gg 1$ we approximate $V(\mathbf{r}) = -V_0 e^{-\hat{k}^2(x^2+y^2)}$ by

$$V(\mathbf{r}) \approx V_0(\hat{k}^2(x^2+y^2) - 1)$$

as $(x, y) \to (0, 0)$, or $(x, y) \to (x_0, y_0)$ where (x_0, y_0) is the coordinate of an arbitrary site. We call this the two quantum dimensional harmonic oscillator, which has been well studied. One can find the results in many books on quantum mechanics (cf. [67]). Below we list some results for formulae that we have used in the above sections.

The 2D harmonic oscillator is the eigenvalue problem

$$\left[\nabla^2 - d_0(x^2+y^2)\right]\eta(\mathbf{r}) = -\epsilon\eta(\mathbf{r}),$$

where $d_0 > 0$ is called the intensity and ϵ the energy. This problem can be solved by separation of variables into two 1D oscillators, by assuming $\eta(x, y) = f(x)g(y)$

$$\left(\frac{d^2}{dx^2} - d_0x^2\right)f(x) = -\epsilon_x f(x),$$

and

$$\left(\frac{d^2}{dy^2} - d_0y^2\right)g(y) = -\epsilon_y g(y),$$

where $\epsilon = \epsilon_x + \epsilon_y$.

Each of the 1D oscillators are solved in terms of Hermite functions; it follows that $\epsilon_x = (1+2m)\sqrt{d_0}$, $m = 0, 1, 2, \ldots$ and the associated normalized eigenfunctions are

$$f_m(x) = \sqrt{\frac{1}{2^m m!}}\frac{d_0^{1/8}}{\pi^{1/4}}e^{-\frac{\sqrt{d_0}}{2}x^2}H_m(d_0^{1/4}x),$$

where $H_m(x)$ is the mth Hermite polynomial. Similarly, $\epsilon_y = (1+2n)\sqrt{d_0}$, $n = 0, 1, 2, \ldots$ and the associated normalized eigenfunctions are

$$g_n(x) = \sqrt{\frac{1}{2^n n!}}\frac{d_0^{1/8}}{\pi^{1/4}}e^{-\frac{\sqrt{d_0}}{2}y^2}H_n(d_0^{1/4}y).$$

So the total eigenvalue is $\epsilon = \epsilon_{m,n} = \sqrt{d_0}[(1+2\,m) + (1+2n)]$ and the associated normalized eigenfunctions are

$$\eta_{m,n}(x, y) = f_m(x)g_n(y),$$

$$= \sqrt{\frac{1}{2^{m+n}m!n!}}\frac{d_0^{1/4}}{\pi^{1/2}}e^{-\frac{\sqrt{d_0}}{2}(x^2+y^2)}H_n(d_0^{1/4}x)H_m(d_0^{1/4}y).$$

We note that the above calculations show that the ground state, or lowest eigenvalue, is simple but the higher ones, e.g the first excited state, can have eigenvalues that are multiple (note that eigenvalue $\epsilon_{1,0} = \epsilon_{0,1}$).

Next, we use the above functions to estimate the parameters for the lowest eigenvalue; i.e., the ground state. As mentioned above, when V_0 is very large, an approximation of $V_s(\mathbf{r})$ is $V_s(\mathbf{r}) = V_0(\hat{k}^2(x^2+y^2) - 1) \approx -V_0 e^{-\hat{k}^2(x^2+y^2)}$. Thus the associated orbitals can be approximated by the wave functions of the harmonic oscillator and the corresponding orbital energy E is approximated by $E = \epsilon - V_0$. There are two parameters: V_0, the depth of the potential and k_0, the width of the potential. The validity of this approximation is due to WKB theory. With the above approximation, $\Delta V(\mathbf{r}) = -V_0\sum_{\mathbf{v}\neq\mathbf{0}} e^{-\hat{k}^2\|\mathbf{r}-\mathbf{v}\|^2}$, where $\|\mathbf{r}\| = \sqrt{x^2+y^2}$ is the standard Euclidean norm. Recall we have assumed that the position of the first site $S_\mathbf{0} = \mathbf{0}$, so $S_\mathbf{v} = \mathbf{v}$. So the square lattice Eq. (4.1) has the asymptotic behavior near the first site $V(\mathbf{r}) \approx V_0\left[\frac{1}{2}k_0^2(x^2+y^2) - 1\right]$ and $V_s(\mathbf{r}) = -V_0 e^{-\frac{k_0^2}{2}(x^2+y^2)}$. The behavior near all other sites is merely a translation of this argument.

As mentioned above, we consider only the lowest band. With the above approximation, the orbital energy and the orbital are

$$E = \epsilon_{0,0} - V_0 = 2\hat{k}\sqrt{V_0} - V_0,$$

$$\phi(\mathbf{r}) = \eta_{0,0}(\mathbf{r}) = \frac{(\hat{k}^2V_0)^{1/4}}{\pi^{1/2}}e^{-\frac{\sqrt{\hat{k}^2V_0}}{2}(x^2+y^2)}.$$

After some further calculations, the parameters in the dispersion relation Eq. (3.5) are found to be

$$\kappa_\mathbf{v} = \int \phi(\mathbf{r})\phi(\mathbf{r}-\mathbf{v})d\mathbf{r} \approx \exp\left(-\frac{1}{4}\hat{k}\sqrt{V_0}\,\|\mathbf{v}\|^2\right),$$

$$\lambda_\mathbf{v} = \int \phi(\mathbf{r})\Delta V(\mathbf{r})\phi(\mathbf{r}-\mathbf{v})d\mathbf{r},$$

$$\approx -\frac{V_0^{3/2}}{\hat{k}+\sqrt{V_0}}\exp\left(-\frac{\hat{k}\sqrt{V_0}(2\hat{k}+\sqrt{V_0})}{4(\hat{k}+\sqrt{V_0})}\|\mathbf{v}\|^2\right),$$

$$\lambda_\mathbf{0} = \int \phi(\mathbf{r})\Delta V(\mathbf{r})\phi(\mathbf{r})d\mathbf{r}$$

$$\approx -\frac{V_0^{3/2}}{\hat{k}+\sqrt{V_0}}\sum_{\langle\mathbf{v}\rangle}\exp\left(-\frac{\hat{k}^2\sqrt{V_0}}{\hat{k}+\sqrt{V_0}}\,\|\mathbf{v}\|^2\right).$$

Since $C_\mathbf{v} = \lambda_\mathbf{v} - \lambda_\mathbf{0}\kappa_\mathbf{v}$,

$$C_\mathbf{v} \approx \frac{V_0^{3/2}}{\hat{k}+\sqrt{V_0}}\exp\left(-\frac{\hat{k}\sqrt{V_0}}{4}\|\mathbf{v}\|^2\right)$$

$$\times\left[\sum_{\langle\mathbf{v}\rangle}\exp\left(-\frac{\hat{k}^2\sqrt{V_0}}{\hat{k}+\sqrt{V_0}}\|\mathbf{v}\|^2\right)\right.$$

$$\left. - \exp\left(-\frac{\hat{k}^2\sqrt{V_0}}{2(\hat{k}+\sqrt{V_0})}\|\mathbf{v}\|^2\right)\right].$$

For simplicity, we only take the leading order of $C_\mathbf{v}$ under the limit $V_0 \gg 1$, and get

$$C_\mathbf{v} \approx V_0\exp\left(-\frac{\hat{k}\sqrt{V_0}}{4}\|\mathbf{v}\|^2\right)\left[\sum_{\langle\mathbf{v}\rangle}\exp\left(-\hat{k}^2\|\mathbf{v}\|^2\right)\right.$$

$$\left. - \exp\left(-\frac{\hat{k}^2}{2}\|\mathbf{v}\|^2\right)\right].$$

As V_0 goes to infinity, $C_\mathbf{v}$ goes to zero exponentially with respect to V_0, while $\lambda_\mathbf{0} \sim O(V_0)$ goes to negative infinity, $E + \lambda_\mathbf{0} \to -\infty$.

Since we consider a square lattice Eq. (4.1) with lattice period ℓ and $\hat{k}^2 = \frac{1}{2}k_0^2$, it follows that

$$C_{\mathbf{v}_1} = C_{\mathbf{v}_2} \approx V_0 \exp\left(-\frac{k_0\sqrt{V_0}\, l^2}{4\sqrt{2}}\right)\left[4\exp\left(-\frac{k_0^2 l^2}{2}\right) - \exp\left(-\frac{k_0^2 l^2}{4}\right)\right].$$

Note that $k_0 l = \pi$, so

$$C_{\mathbf{v}_1} = C_{\mathbf{v}_2} \approx -0.056 V_0 \exp\left(-\frac{\sqrt{V_0}\,\pi^2}{4\sqrt{2}k_0}\right).$$

6. A typical non-simple lattice—honeycomb lattice

As mentioned earlier, a non-simple lattice may have more than one site, i.e., one minima, in a unit cell. In this case one may need more than one initial site to describe the lattice. An example of a non-simple lattice is the honeycomb lattice. The right-hand lattice in Fig. 6 is a non-simple honeycomb lattice. Its sites (potential minima) consist of 'black' and 'white' sites. The black and white sites are separately constructed from the underlying primitive vectors. Hence, we need two initial sites to describe the honeycomb lattice.

A perfect hexagonal lattice is composed of two standard triangular sublattices: A and B sublattices. The lattice vectors $\mathbb{P}$ should form a triangular lattice. To generate the other sublattice, extra information is needed to determine the shift from the B site to the A site in the same unit cell. We denote this shift as a vector $\mathbf{d}_1$. The lattice vectors are given by $\mathbf{v}_1$ and $\mathbf{v}_2$, and a displacement between adjacent A and B sites is $\mathbf{d}_1 = -\frac{1}{3}(\mathbf{v}_1 + \mathbf{v}_2)$. We also introduce two other vectors. $\mathbf{d}_2 = \mathbf{v}_2 + \mathbf{d}_1$ $\mathbf{d}_3 = \mathbf{v}_1 + \mathbf{d}_1$. The vectors and their relations are shown in Fig. 8. By connecting all the nearest neighbors, a perfect hexagonal lattice is obtained. It is noted that all A (filled-black) form a triangular sublattice and all B (open-white) sites form the other triangular sublattices. The distance between two nearest A sites or two nearest B sites (next-nearest neighbors) is l. However, the nearest neighbors of A sites are three B sites are a distance $l/\sqrt{3}$ apart and the shifts are determined by $\mathbf{d}_1$, $\mathbf{d}_2$ and $\mathbf{d}_3$.

A honeycomb lattice can be constructed by three interfering plane waves

$$V(\mathbf{r}) = \frac{V_0}{9}\left(\left|e^{ik_0\mathbf{b}_1\cdot\mathbf{r}} + e^{ik_0\mathbf{b}_2\cdot\mathbf{r}} + e^{ik_0\mathbf{b}_3\cdot\mathbf{r}}\right|^2 - 9\right), \tag{6.1}$$

where $0 \geq V(\mathbf{r}) \geq -V_0$ and $\mathbf{b}_1 = (0, 1)$, $\mathbf{b}_2 = (-\frac{\sqrt{3}}{2}, -\frac{1}{2})$ and $\mathbf{b}_3 = (\frac{\sqrt{3}}{2}, -\frac{1}{2})$; $V_0 > 0$ is the lattice intensity; k_0 is the scaled wavelength of the interfering plane waves. The characteristic vectors for this potential are

$$\mathbf{v}_1 = l\left(\frac{\sqrt{3}}{2}, \frac{1}{2}\right), \qquad \mathbf{v}_2 = l\left(\frac{\sqrt{3}}{2}, -\frac{1}{2}\right);$$

$$\mathbf{k}_1 = \frac{4\pi}{\sqrt{3}l}\left(\frac{1}{2}, \frac{\sqrt{3}}{2}\right), \qquad \mathbf{k}_2 = \frac{4\pi}{\sqrt{3}l}\left(\frac{1}{2}, -\frac{\sqrt{3}}{2}\right),$$

where $l = \frac{4\pi}{3k_0}$ and $\mathbf{v}_i \cdot \mathbf{k}_j = 2\pi\delta_{ij}$ The lattice in Eq. (6.1) has the periodicity $V(\mathbf{r} + m\mathbf{v}_1 + n\mathbf{v}_2) = V(\mathbf{r})$ for any $m, n \in \mathbb{Z}$.

As earlier, the dispersion relation is determined from Eq. (2.3). For a honeycomb lattice it is convenient to write the potential in the form

$$V(\mathbf{r}) = \sum_{\mathbf{v}} [V_A(\mathbf{r} - \mathbf{v}) + V_B(\mathbf{r} - \mathbf{v})] \tag{6.2}$$

where V_A, V_B denote the potentials generated from the two sites in the primitive unit cell. In the tight-binding approximation they have sharp minima near the A and B sites, respectively; the sum over $\mathbf{v}$ means $\mathbf{v}$ takes all values in $\mathbb{P}$, i.e., $\mathbf{v} = m\mathbf{v}_1 + n\mathbf{v}_2$, for all $m, n \in \mathbb{Z}$. The Bloch mode is assumed to take the form

$$\varphi(\mathbf{r}; \mathbf{k}) = a\sum_{\mathbf{v}} \phi_A(\mathbf{r} - \mathbf{v})e^{i\mathbf{k}\cdot\mathbf{v}} + b\sum_{\mathbf{v}} \phi_B(\mathbf{r} - \mathbf{v})e^{i\mathbf{k}\cdot\mathbf{v}}$$

where $\phi_A(\mathbf{r})$ and $\phi_B(\mathbf{r})$ represent an orbital (i.e., Wannier function) of a single V_A or V_B potential, respectively; they have the same eigenvalue denoted as E. That is to say,

$$\left[\nabla^2 - V_j(\mathbf{r})\right]\phi_j(\mathbf{r}) = -E\phi_j(\mathbf{r}), \tag{6.3}$$

where j is A or B. Here we only consider the lowest band energy level, so there is no subindex to denote different bands. We also assume ϕ_A and ϕ_B are real and normalize them with norm 1, i.e., $\int \phi_A^2 d\mathbf{r} = \int \phi_B^2 d\mathbf{r} = 1$. It is convenient to introduce the

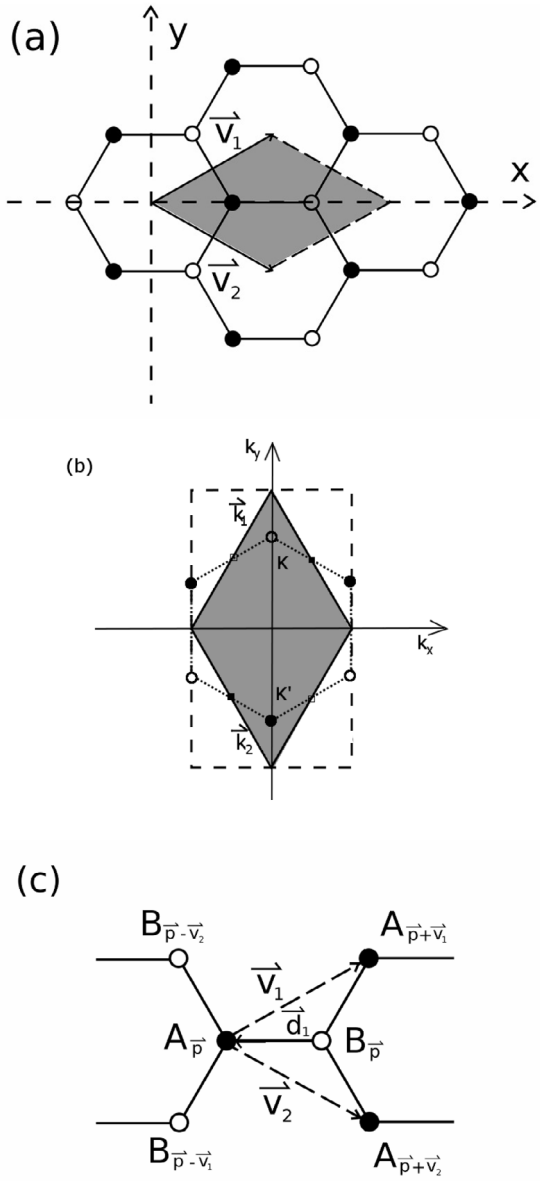

Fig. 8. The hexagonal lattice (a) and the extended Brillouin zone (b). Shaded regions in (a) and (b) are the unit cell Ω and reciprocal unit cell Ω', respectively. The construction of the A (filled-black) and B (open-white) sublattices is also depicted (c).

notation

$$\Delta V_j(\mathbf{r}) = V(\mathbf{r}) - V_j(\mathbf{r}) = \sum_{\mathbf{v}\neq\mathbf{0}} \left[V_j(\mathbf{r}-\mathbf{v}) + V_l(\mathbf{r}-\mathbf{v})\right] + V_l(\mathbf{r}),$$

for $l \neq j$. Again, we consider the tight-binding limit, i.e., $V_0 \gg 1$ which means the potential well at each site is very deep, and only on-site and nearest neighbor interactions will need to be considered [62].

6.1. Dispersion relation

As in the simple lattice case, we first determine the dispersion relation. We can use Fredholm alternative conditions or equivalently the following method. Substituting the above Bloch mode $\varphi(\mathbf{r};\mathbf{k})$ into the eigenproblem Eq. (2.3), and applying the orbital relation in Eq. (6.3), we get

$$\sum_{\mathbf{v}} [(\mu - E)[a\phi_A(\mathbf{r}-\mathbf{v}) + b\phi_B(\mathbf{r}-\mathbf{v})] - a\Delta V_A(\mathbf{r}-\mathbf{v})\phi_A(\mathbf{r}-\mathbf{v}) - b\Delta V_B(\mathbf{r}-\mathbf{v})\phi_B(\mathbf{r}-\mathbf{v})]\, e^{i\mathbf{k}\cdot\mathbf{v}} = 0. \quad (6.4)$$

Multiplying $\phi_j(\mathbf{r}), j = A, B$ to Eq. (6.4) and integrating over the whole plane, we get the matrix eigenvalue problem,

$$\begin{pmatrix} \mu - E - c_0 & [(\mu - E)c_1 - c_2]\gamma(\mathbf{k}) \\ [(\mu - E)c_1 - c_2]\,\gamma^*(\mathbf{k}) & \mu - E - c_0 \end{pmatrix} \begin{pmatrix} a \\ b \end{pmatrix} = \begin{pmatrix} 0 \\ 0 \end{pmatrix}. \quad (6.5)$$

Here only on-site and nearest neighbor interactions are considered because of the tight-binding limit; and

$$\gamma(\mathbf{k}) = (1 + e^{-i\mathbf{k}\cdot\mathbf{v}_1} + e^{-i\mathbf{k}\cdot\mathbf{v}_2})$$

$$c_0 = \int \phi_A(\mathbf{r})\Delta V_A(\mathbf{r})\phi_A(\mathbf{r})d\mathbf{r} = \int \phi_B(\mathbf{r})\Delta V_B(\mathbf{r})\phi_B(\mathbf{r})d\mathbf{r};$$

$$c_1(\|\mathbf{v}\|) = \int \phi_A(\mathbf{r})\phi_B(\mathbf{r}-\mathbf{v})d\mathbf{r} = \int \phi_B(\mathbf{r})\phi_A(\mathbf{r}-\mathbf{v})d\mathbf{r};$$

$$c_2(\|\mathbf{v}\|) = \int \phi_A(\mathbf{r})\Delta V_B(\mathbf{r}-\mathbf{v})\phi_B(\mathbf{r}-\mathbf{v})d\mathbf{r} = \int \phi_B(\mathbf{r})\Delta V_A(\mathbf{r}-\mathbf{v})\phi_A(\mathbf{r}-\mathbf{v})d\mathbf{r}.$$

It is noted that c_0, c_1, c_2 are all real and c_1 and c_2 are very small. Moreover, the coefficients c_1 and c_2 are functions of the distance $\|\mathbf{v}\|$, and as a result, each nearest neighbor term is identical, up to a phase. Note we can use $V_B(\mathbf{r}) = V_A(\mathbf{r}-\mathbf{d}_1)$ and $\phi_B(\mathbf{r}) = \phi_A(\mathbf{r}-\mathbf{d}_1)$ in these calculations.

The system in Eqs. (6.5) has non-trivial solutions if and only if the determinant is zero. The dispersion relation that follows is

$$\mu(\mathbf{k}) - E - c_0 = \pm|(\mu(\mathbf{k}) - E)c_1 + c_2| \cdot |\gamma(\mathbf{k})|.$$

Since $c_1, c_2 \ll 1$, the above dispersion relation becomes (higher order terms are omitted)

$$\mu(\mathbf{k}) \approx E + c_0 \pm C|\gamma(\mathbf{k})|,$$

where $C = c_0c_1 - c_2$. Since the asymptotic behavior of the honeycomb potential Eq. (6.1) near the site is $V(\mathbf{r}) \approx -V_0(\frac{1}{4}k_0^2((x - x_0)^2 + (y - y_0)^2) - 1)$, we can find that $C = -0.297V_0e^{-\frac{2\sqrt{V_0}\pi^2}{9k_0}} < 0$ with the same approximations we used in the simple lattice case.

A typical dispersion surface containing the two lowest spectral bands is depicted in the left hand Fig. 9; an intensity plot of a hexagonal lattice is given in the right side. The touching points, also referred to as Dirac points, correspond to the zeros of $\gamma(\mathbf{k})$.

It is also known that material graphene has honeycomb lattice structure. In the graphene literature, it has been shown that

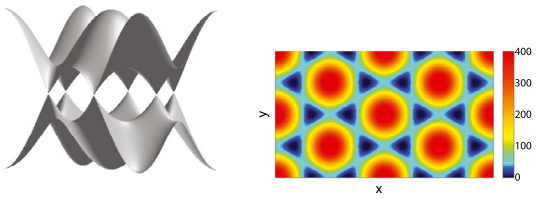

Fig. 9. Left: the two lowest spectral bands of a typical honeycomb lattice. The touching points are the Dirac points [26]. Right: an intensity plot of potential (6.1). The local minima (blue) are identified as sites. The local maxima are at the centers of a triangular lattice of hexagons.

two different energy bands can touch each other at certain isolated points that are called Dirac points; such Dirac points are sometimes termed diabolical points [28,68]. Thus Dirac points also exist in the band structure of two-dimensional honeycomb lattices. The tight-binding approximation is often used in the study of graphene and it is found that structure of the dispersion relation near these Dirac points is conical in nature [69,70]; the regions in the neighborhood of Dirac points are called Dirac cones.

Note that $\gamma(\mathbf{k})$ is periodic in $\mathbf{k}$. In one reciprocal unit cell, there are two zeros known as Dirac points, which we denote K and K'. For the above special potential Eq. (6.1), the location of the Dirac points are

$$K = \left(0, \frac{4\pi}{3l}\right) \quad \text{and} \quad K' = \left(0, -\frac{4\pi}{3l}\right). \quad (6.6)$$

All the zeros of $\gamma(\mathbf{k})$ form the reciprocal hexagonal lattice, which also happens to be the Brillouin zone. At these points, $\mu - E - c_0 = 0$ and so the matrix in Eq. (6.5) is identically equal zero. Thus, a and b are free. Thus the eigenspace is two dimensional. The associated original linear Schrödinger eigenproblem has degeneracy. In other words, when $\mu = E + c_0$, the eigenproblem Eq. (2.3) has two independent Bloch modes.

6.2. Envelope dynamics

Suppose we input a Bloch wave envelope into the crystal. To leading order, the envelope is taken to vary slowly along z,

$$\psi \sim \left(\sum_{\mathbf{v}} a_{\mathbf{v}}(Z)\phi_A(\mathbf{r}-\mathbf{v})e^{i\mathbf{k}\cdot\mathbf{v}} + \sum_{\mathbf{v}} b_{\mathbf{v}}(Z)\phi_B(\mathbf{r}-\mathbf{v})e^{i\mathbf{k}\cdot\mathbf{v}}\right)e^{-i\mu z}. \quad (6.7)$$

Since ψ is not a Bloch mode anymore, the intensities are different at different sites, i.e., a and b have subindex $\mathbf{v}$ that are sites on the A,B lattices, respectively, and $Z = \varepsilon z$; the small parameter ε will be determined later.

Substituting the envelope solution Eq. (6.7) into the lattice NLS Eq. (2.1), one obtains

$$\begin{aligned} &\sum_{\mathbf{v}}\Big(\varepsilon i\frac{da_{\mathbf{v}}}{dZ} + a_{\mathbf{v}}\Big[\nabla^2 - V(\mathbf{r}-\mathbf{v})\Big]\phi_A(\mathbf{r}-\mathbf{v}) \\ &+ \mu a_{\mathbf{v}}\phi_A(\mathbf{r}-\mathbf{v})\Big)e^{i\mathbf{k}\cdot\mathbf{v}} \\ &+ \sum_{\mathbf{v}}\Big(\varepsilon i\frac{db_{\mathbf{v}}}{dZ} + b_{\mathbf{v}}\Big[\nabla^2 - V(\mathbf{r}-\mathbf{v})\Big]\phi_B(\mathbf{r}-\mathbf{v}) \\ &+ \mu b_{\mathbf{v}}\phi_B(\mathbf{r}-\mathbf{v})\Big)e^{i\mathbf{k}\cdot\mathbf{v}} \\ &+ \sigma\left(\sum_{\mathbf{v}}(a_{\mathbf{v}}(Z)\phi_A(\mathbf{r}-\mathbf{v}) + b_{\mathbf{v}}(Z)\phi_B(\mathbf{r}-\mathbf{v}))\,e^{i\mathbf{k}\cdot\mathbf{v}}\right)^2 \\ &\times\left(\sum_{\mathbf{v}}(a_{\mathbf{v}}(Z)\phi_A(\mathbf{r}-\mathbf{v}) + b_{\mathbf{v}}(Z)\phi_B(\mathbf{r}-\mathbf{v}))\,e^{i\mathbf{k}\cdot\mathbf{v}}\right)^* = 0. \end{aligned} \quad (6.8)$$

To simplify the steps, rather than employing Fredholm conditions, we can do the following. Multiply $\phi_j(\mathbf{r}-\mathbf{p})e^{-i\mathbf{k}\cdot\mathbf{p}}, j=A,B$, where $\mathbf{p}\in\mathbb{P}$, to Eq. (6.8) and integrate over the whole plane to get

$$\varepsilon i\frac{da_{\mathbf{p}}}{dZ}+(\mu-E-c_0)a_{\mathbf{p}}+[(\mu-E)c_1-c_2]\mathcal{L}_1 b_{\mathbf{p}}+\sigma g|a_{\mathbf{p}}|^2a_{\mathbf{p}}=0;$$
$$\varepsilon i\frac{db_{\mathbf{p}}}{dZ}+(\mu-E-c_0)b_{\mathbf{p}}+[(\mu-E)c_1-c_2]\mathcal{L}_2 a_{\mathbf{p}}+\sigma g|b_{\mathbf{p}}|^2b_{\mathbf{p}}=0,$$

where

$$\mathcal{L}_1 b_{\mathbf{p}}=b_{\mathbf{p}}+b_{\mathbf{p}-\mathbf{v}_1}e^{-i\mathbf{k}\cdot\mathbf{v}_1}+b_{\mathbf{p}-\mathbf{v}_2}e^{-i\mathbf{k}\cdot\mathbf{v}_2},$$
$$\mathcal{L}_2 a_{\mathbf{p}}=a_{\mathbf{p}}+a_{\mathbf{p}+\mathbf{v}_1}e^{i\mathbf{k}\cdot\mathbf{v}_1}+a_{\mathbf{p}+\mathbf{v}_2}e^{i\mathbf{k}\cdot\mathbf{v}_2},$$

and $g=\int\phi_A^4d\mathbf{r}=\int\phi_B^4d\mathbf{r}$. Recall that $c_1=c_1(\|\mathbf{v}\|)$ and $c_2=c_2(\|\mathbf{v}\|)$, that is the coefficients are functions of distance with respect to a displacement vector $\mathbf{v}$.

Away from the Dirac points, the situation is essentially the same as in the simple lattice. Here the determinant of the system Eqs. (6.5) is nonzero and $a_{\mathbf{p}}$ is proportional to $b_{\mathbf{p}}$ and the equations reduce to those discussed earlier in the simple lattice case. So, next we only consider the case when we are near Dirac points, so that $\mathbf{k}$ takes the value near K, for example. At that point, considering $\mu-E-c_0=0$, the envelope equation is, after rescaling (recall $C<0$),

$$i\frac{da_{\mathbf{p}}}{dZ}+\mathcal{L}_1 b_{\mathbf{p}}+s(\sigma)|a_{\mathbf{p}}|^2a_{\mathbf{p}}=0; \tag{6.9}$$
$$i\frac{db_{\mathbf{p}}}{dZ}+\mathcal{L}_2 a_{\mathbf{p}}+s(\sigma)|b_{\mathbf{p}}|^2b_{\mathbf{p}}=0, \tag{6.10}$$

where we have taken $\varepsilon\sim O(|C|)\sim O(|\sigma|)$ to ensure maximal balance and again $s(\sigma)$ is the sign of σ, or zero if there is no nonlinearity. The system (6.9)–(6.10) is what we refer to as the discrete Dirac system.

6.3. Continuum reduction

Next we consider the continuous limit; i.e., we assume the lattice constant l is much smaller than the characteristic scale of the envelope. Denote $a(\mathbf{R})$ and $b(\mathbf{R})$ as the continuous envelopes where $\mathbf{R}=(X,Y)=\nu\mathbf{r}$, $\nu\ll 1$. Then after some expansions at the Dirac point $\mathbf{k}=K$, similar to Eq. (3.11), we obtain $\mathcal{L}_1\approx\frac{\nu\sqrt{3}l}{2}(\partial_X+i\partial_Y)$ and $\mathcal{L}_2\approx\frac{\nu\sqrt{3}l}{2}(-\partial_X+i\partial_Y)$. Note that expanding around the other Dirac point, $\mathbf{k}=K'$, results in the conjugate system with $\mathcal{L}_1\approx\frac{\nu\sqrt{3}l}{2}(\partial_X-i\partial_Y)$ and $\mathcal{L}_2\approx\frac{\nu\sqrt{3}l}{2}(-\partial_X-i\partial_Y)$. Thus the discrete system near $\mathbf{k}=K$ becomes the following continuous Dirac system (after rescaling)

$$i\frac{da}{dZ}+(\partial_X-i\partial_Y)b+s(\sigma)|a|^2a=0; \tag{6.11}$$
$$i\frac{db}{dZ}+(-\partial_X-i\partial_Y)a+s(\sigma)|b|^2b=0, \tag{6.12}$$

where we have taken $\varepsilon\sim O(|C|\nu)\sim O(|\sigma|)$ to ensure the maximal balance. The continuous Dirac system governs broad envelopes of Bloch modes with quasimomentum $\mathbf{k}=K$ propagating in the honeycomb lattice. If the envelope is not wide, i.e., not slowly varying in the transverse direction, the discrete system is more appropriate than the continuous system to describe the envelope evolution. If the envelope is very wide, both discrete and continuous systems are satisfactory, but the continuous system is simpler to use. Finally, observe that combining the linearized version of system (6.11)–(6.12) yields the 2D wave equation

$$\frac{\partial^2a}{\partial Z^2}=\frac{\partial^2a}{\partial X^2}+\frac{\partial^2a}{\partial Y^2},$$

with wave speed 1.

We can compare typical numerical simulations of both lattice NLS equation and the Dirac system. The comparison between magnitudes is displayed in Fig. 10. The top panel is from the lattice NLS equation and the bottom panel is from the Dirac system. From the top panel, we see that a spot becomes two rings that separated by a dark ring. The simulation of the Dirac system gives an excellent match. Thus the Dirac system is a good model to describe the envelope of Bloch modes near a Dirac point propagating in a perfect hexagonal lattice. The system (6.9)–(6.10) was originally found in [18].

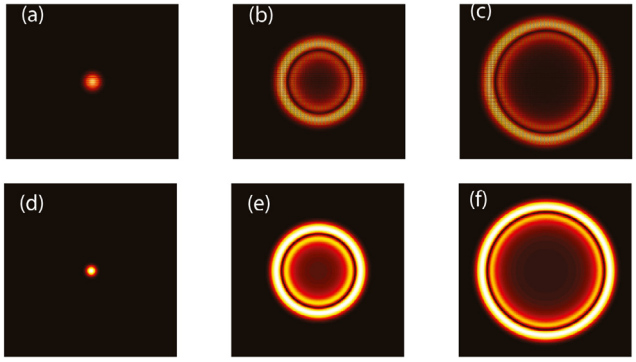

Fig. 10. The propagation of the magnitude of a Gaussian Bloch mode envelope associated with a Dirac point. Top: simulations of the lattice NLS Eq. (2.1); Bottom: simulations of the Dirac Eqs. (6.11) and (6.12); here only the A-component is shown. Reprinted figure with permission from [52], copyright (2010) by the American Physical Society.

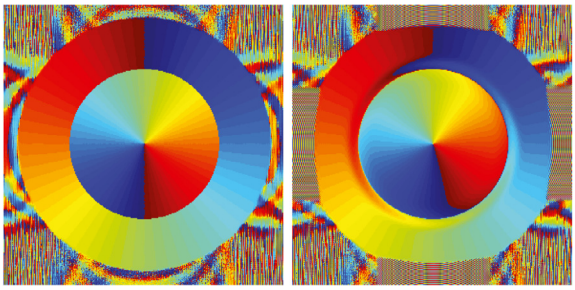

Fig. 11. Left: phase structure of amplitude A in linear Dirac system; Right: phase structure of the amplitude A in the nonlinear system. Reprinted figure with permission from [18], copyright (2009) by the American Physical Society.

Thus the existence of Dirac points shows us that certain envelopes associated with the underlying Bloch modes propagate in an interesting manner: an input spot becomes two expanding bright rings as the beam propagates in the crystal. This phenomenon is called conical diffraction [28,68] and is a fundamental feature of crystal optics and is of interest in mathematics and physics. It was first predicted by W. Hamilton [71] in 1832 and observed by H. Lloyd [72] in a biaxial crystal soon afterwards; here a narrow beam entering a crystal spreads into a hollow cone within the crystal. The existence of the conical diffraction phenomenon in the light beam propagation in honeycomb lattices was demonstrated both experimentally and numerically in [27, 73]. The theoretical explanation was given shortly thereafter [18].

We mention that for both the linear and nonlinear lattices the evolution of the magnitude (recall Fig. 10) is similar and we observe conical diffraction. However, there is some difference in the phase structure—above we used amplitude A. This is indicated in Fig. 11 where the left figure is associated with a linear lattice and the right figure a nonlinear lattice (see [18,52,74]). When the honeycomb lattice is deformed, then we can have elliptical and even straight line diffraction [75]. The system of envelope equations changes significantly when one considers shallow lattices [76].

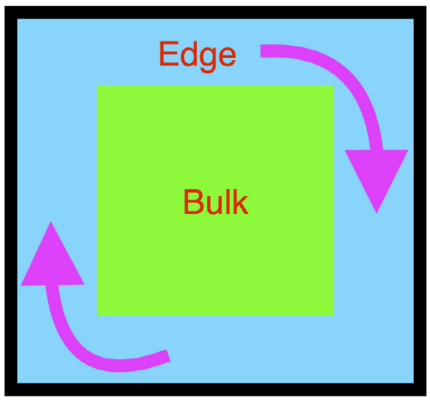

Fig. 12. Edge mode propagation along the boundary of a 2D domain. The bulk region is in the middle, separated from the domain walls.

7. Topological insulator systems

Within the framework of the lattice waveguides described above, it is possible to realize topological insulator systems. Generally speaking, topological insulators behave as insulators (forbid flow of energy) in the bulk or interior of a medium, but act as conductors (allow flow of energy) along the edge or surface. Localized states, called edge modes, decay exponentially fast perpendicular to the medium boundary and propagate parallel to it [77]; see e.g. Fig. 12. Moreover, these edge states can be associated with topological invariants. In the case of a nontrivial topological invariant, the bulk-edge correspondence implies the existence of topologically-protected modes. These modes tend to be unusually robust and retain their form, even when they propagate into/around a material defect.

Two different systems will be presented, each with its own characteristics. The first is the 1D Su–Schrieffer–Heeger (SSH) model, originally used to understand the propagation of solitary waves in hydrocarbon chains [78]. The SSH model is similar to the 1D discrete NLS model in Eq. (3.10), except the left and right couplings are not equal. The second system is a 2D Floquet topological insulator, which can be realized in photonic lattices by longitudinal modulation of a waveguide array [37]. In terms of the governing equations, this results in time-dependent coefficients, which can be solved via Floquet theory.

One of the necessary ingredients for inducing modes with nontrivial topological invariants is the breaking of symmetries. In the case of the SSH model, inversion symmetry is broken by the asymmetric coefficient values. In the case of Floquet photonic insulator, the temporal driving breaks time-reversal symmetry by the time-dependent coefficients. Symmetry breaking can open spectral band gaps that admit topologically-protected modes.

It is possible to find parameter regimes where the corresponding bulk eigenmodes of these systems acquire nontrivial topological invariants. The topological invariants considered here are defined in terms of line integrals in their associated spectral planes. These integrals are indirect ways of determining whether or not the modes possess nontrivial phase properties. For the SSH model, the eigenmodes can possess a nonzero Zak phase [79], which corresponds to a winding number of the phase. In the Floquet model, eigenstates can acquire a nonzero Chern number [33], which is related to the Berry phase [80] that indicates a phase discontinuity.

A consequence of a nontrivial topological invariant is remarkably stable modes, known as topologically protected modes. The SSH modes are localized at the endpoints of the lattice, and remain fixed throughout the evolution. On the other hand, the Floquet edge modes with nonzero Chern number propagate unidirectionally along the boundary and around any defects they encounter. Rather than backscatter, as one might expect, here there is unidirectional mode propagation. This propagation in a preferred orientation is known as chirality.

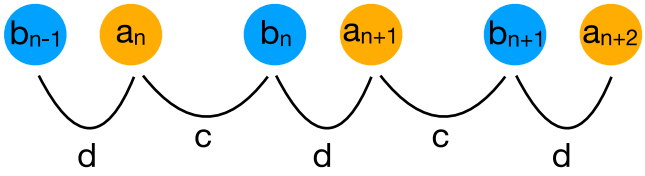

Fig. 13. 1D SSH lattice waveguide profiles. Nearest neighbor couplings are indicated. Here, $d > c > 0$ due to the spacing.

The connection between the bulk topological invariants and topologically protected edges states is the bulk-edge correspondence (see [81–84]). The principle typically consists of the following properties: (1) A chiral edge mode exists for a topological insulators if the corresponding bulk modes have a non-zero topological invariant. (2) The topological number is equal to the net number of chiral edge states. (3) The topological invariant is independent of surface defects or boundary conditions.

8. The SSH waveguide lattice

The simplest topological insulator system to realize in a photonic waveguide system is that of the SSH model. The model can be formulated by adjusting the waveguide spacings in an alternating manner, like that in Fig. 13. Experimentally, these types of lattices have been realized in laser-etched arrays [85] and photorefractive crystals [86].

We assume that the potential minima $V(\mathbf{r})$ and orbital approximation near both a and b lattice sites are of identical form. As a result, the coupling coefficients, which are inversely proportional to distance, are asymmetric. After transforming and rescaling a set of equations similar to Eq. (3.10), one obtains the nonlinear SSH system in Kerr media

$$i\frac{da_n}{dz} + cb_n + db_{n-1} + \gamma|a_n|^2 a_n = 0 \tag{8.1}$$

$$i\frac{db_n}{dz} + ca_n + da_{n+1} + \gamma|b_n|^2 b_n = 0 \tag{8.2}$$

where $n \in \mathbb{Z}$ and c, d, γ are taken to be non-negative coefficients. If $c > d$, this physically corresponds to placing the waveguides a_n and b_n closer together than their other neighbors; and vice versa if $c < d$ see e.g. Fig. 13. By allowing $c \neq d$, the inversion symmetry of the problem, $V(\mathbf{r}) = V(-\mathbf{r})$, is broken, unlike the simple square lattice examined in Section 4.

Some of the main results associated with the SSH model are presented below; a more comprehensive treatment can be found in [81]. To highlight the topological nature of this system, consider plane wave solutions on the infinite line domain of the form

$$\begin{pmatrix} a \\ b \end{pmatrix}_n = \begin{pmatrix} \alpha \\ \beta \end{pmatrix}(k)\, e^{i(kn-\lambda z)}.$$

In the linearized problem ($\gamma = 0$), this yields the eigenvalue system

$$\mathcal{H}(k)\mathbf{c} = -\lambda\mathbf{c}, \qquad \mathbf{c} = \begin{pmatrix} \alpha \\ \beta \end{pmatrix} \tag{8.3}$$

for (the spectral Hamiltonian)

$$\mathcal{H}(k) = \begin{pmatrix} 0 & c + de^{-ik} \\ c + de^{ik} & 0 \end{pmatrix},$$

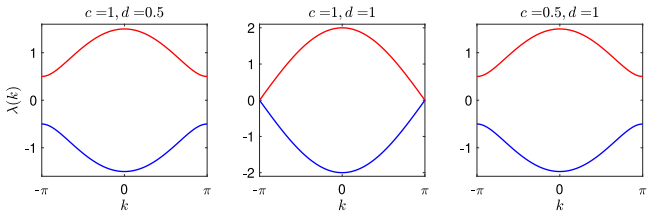

Fig. 14. SSH model bulk dispersion relations in Eq. (8.4).

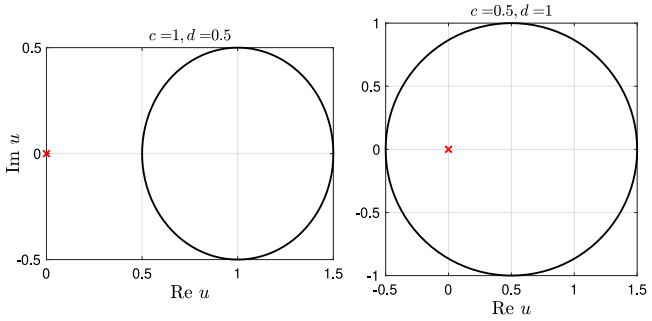

Fig. 15. Path of complex function $u(k) = c + de^{-ik}$ for $k \in [0, 2\pi]$. Note that the loop is clockwise oriented.

which is 2π-periodic in k. The two dispersion relations are given by

$$\lambda_{\pm}(k) = \pm\left|c + de^{-ik}\right|, \tag{8.4}$$

leading to a gap width of $2|c - d|$. The corresponding normalized eigenfunctions are

$$\mathbf{c}_{\pm}(k) = \frac{1}{\sqrt{2}}\begin{pmatrix} \mp e^{i\theta(k)} \\ 1 \end{pmatrix}, \tag{8.5}$$

where $\theta(k) = \tan^{-1}\left(-\frac{d\sin k}{c+d\cos k}\right)$ is the counterclockwise angle from the positive real axis. A plot of the dispersion relations for different values of c and d is shown in Fig. 14. Notice that when inversion symmetry is broken ($c \neq d$), a gap opens between the bands. When the symmetry is preserved ($c = d$), the gap closes at $k = \pm\pi$.

The topological quantity associated with this system is the Berry/Zak phase

$$\mathcal{Z} = i\oint \left\langle \mathbf{c} \left| \frac{\partial \mathbf{c}}{\partial k} \right\rangle dk, \tag{8.6}$$

where $\langle \mathbf{f}|\mathbf{g}\rangle = \mathbf{f}^{\dagger}\mathbf{g}$ and $\dagger$ denotes the complex conjugate transpose. The Zak phase is an indirect way of measuring the winding number of the eigenfunction phase $\theta(k)$ over one period in k. To see this, take the eigenfunction in Eq. (8.5) and observe that

$$\mathcal{Z} = i\oint \left\langle \mathbf{c}_{\pm} \left| \frac{\partial \mathbf{c}_{\pm}}{\partial k} \right\rangle dk = \frac{i}{2}\int_0^{2\pi} i\frac{d\theta}{dk}dk = -\frac{1}{2}\theta(k)\Big|_{k=0}^{k=2\pi}.$$

A graphical depiction of the path $c + de^{-ik}$ for topologically distinct parameter sets is shown in Fig. 15. In the topological case ($d > c$), the path encircles the origin and corresponds to a Zak phase of $\mathcal{Z} = -\frac{1}{2}[\theta(2\pi) - \theta(0)] = -\frac{1}{2}[-2\pi - 0] = \pi$. On the other hand, in the non-topological case ($d < c$), the loop does not enclose the origin and $\mathcal{Z} = -\frac{1}{2}[0 - 0] = 0$.

Now let us examine the finite domain problem, which may support edge modes. Here the topological (nonzero Zak phase) case corresponds to localized chiral edge modes at the endpoints of the lattice (recall the bulk-edge correspondence). We impose

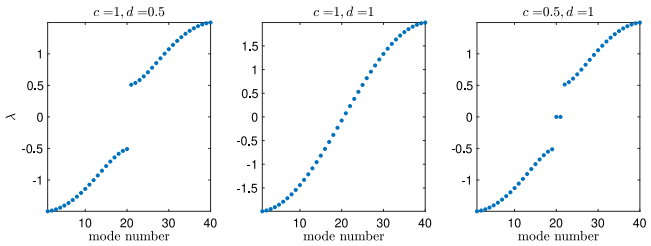

Fig. 16. SSH model edge dispersion relations in Eq. (8.7) using $N = 20$ sites. Recall that $c > d$ ($c < d$) corresponds to the non-topological (topological) case in Fig. 15.

the Dirichlet zero boundary conditions

$$a_n, b_n = 0, \quad \text{for} \quad n < 1 \text{ and } n > N$$

in the linearized version of Eq. (8.1) with $N \gg 1$. For time-harmonic solutions of the form $a_n(t) = \alpha_n e^{-i\lambda t}$ and $b_n(t) = \beta_n e^{-i\lambda t}$ The corresponding system is given by

$$\mathbb{M}\mathbf{c}_n = -\lambda \mathbf{c}_n \tag{8.7}$$

where $\mathbb{M}$ is the $2N \times 2N$ matrix

$$\mathbb{M} = \left(\begin{array}{c|c} O & \mathcal{M} \\ \hline \mathcal{M}^T & O \end{array}\right), \quad \mathcal{M} = \begin{pmatrix} c & & & \\ d & c & & \\ & d & \ddots & \\ & & \ddots & \\ & & & d \quad c \end{pmatrix},$$

O is a zero matrix and $\mathbf{c}_n = (\alpha_1, \alpha_2, \ldots, \alpha_N \mid \beta_1, \beta_2, \ldots, \beta_N)^T$. The solution of system (8.7) for different parameter values is shown in Fig. 16. Noticeably, when $c > d$ (non-topological case) there are no localized edge modes. On the other hand, when $d > c$ (topological case) there are two zero energy ($\lambda = 0$) edge states. Via the bulk-edge correspondence, we infer that these eigenmodes correspond to a chiral edge state.

Plots of the eigenmodes are shown in Fig. 17. There are two zero energy, localized eigenmodes: symmetric and anti-symmetric; both are real. Analytically, one can show that the zero energy modes along the left edge are of the form

$$a_n(t) = \left(-\frac{c}{d}\right)^n, \qquad b_n(t) = 0, \tag{8.8}$$

and decay as $n \to \infty$ when $c < d$. A similar form exists on the right edge, except the b_n mode is decaying and a_n is zero. All other nonzero energy modes are bulk modes and they are not localized.

Physically speaking, the presence of edges modes corresponds to isolated endpoints in Fig. 13, well-separated from the next interior site. In the topological regime, the mode propagation manifests itself as an electromagnetic field concentrated at the endpoints.

Theoretical and experimental research on the nonlinear SSH model is still ongoing. A number of works have established the existence of nonlinear solitons for the system (8.1) in the bulk [87–89] and at the edge [90,91]. Topological edge solitons appear rather stable, as long as the energies are well-removed from the balanced limit, $c \approx d$ [91]. We point out that with non-Kerr type nonlinearities, fascinating phenomena such as nonlinear-induced topological transition [92,93] have been theorized.

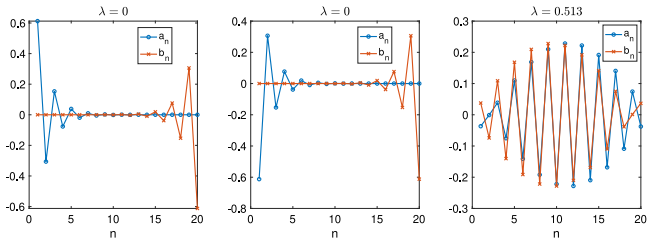

Fig. 17. SSH edge eigenmodes of Eq. (8.7) using $N = 20$ sites and $c = 0.5, d = 1$ (topological case). The corresponding eigenvalues are shown in Fig. 16. All eigenmodes are real.

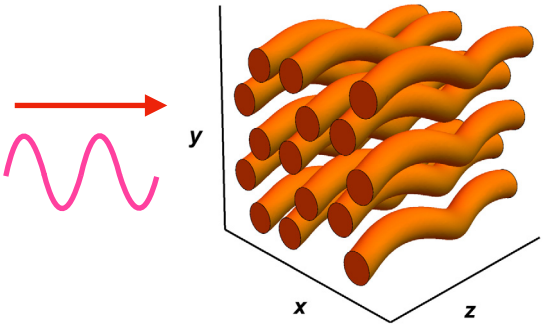

Fig. 18. An electromagnetic wave propagating through a honeycomb lattice that is helically-varying in the longitudinal direction. The lattice rods correspond to regions of higher index of refraction and act as waveguides.

9. Longitudinally-driven photonic lattices

A photonic Floquet topological insulator is described in this section. The proposal and experimental realization of this system was originally given in the seminal work of Rechtsman et al. [37]. Physically, the system is a photonic waveguide array, similar to the one described in Section 1. The new technique introduced is that the waveguides are constructed with a helical-variation in the longitudinal direction (see Fig. 18). As a result, one obtains lattice potentials that are periodic in both the transverse *and* longitudinal directions. Lattices that are periodic in the time (or time-like) variable are typically referred to as *Floquet lattices* due to the classic mathematical theory of ODEs developed by Floquet [59]. Below, the key ideas and governing equations are described; a more thorough treatment can be found in [40–42].

The starting point is a modification of Eq. (2.1), now with a longitudinally-varying photonic lattice that is modeled by the potential $V(\mathbf{r}, z)$ that is periodic in x, y, and z. The governing equation is

$$i\psi_z + \nabla^2\psi - V(\mathbf{r}, z)\psi + \sigma|\psi|^2\psi = 0, \tag{9.1}$$

where $V(\mathbf{r}, z) = V(\mathbf{r} - \mathbf{h}(z))$ for the potential given in Eq. (2.7), with driving function $\mathbf{h}(z)$ that has period T: $\mathbf{h}(z + T) = \mathbf{h}(z)$. Physically, this corresponds to waveguides where the lattice sites oscillate with a helical motion in z. In [41,42] more complicated lattice driving patterns were considered in which each sublattice was allowed to move independently, as long as there was a commensurate period. Here, however, we only consider the case where all lattice sites are driven in the same manner.

A natural transformation is to the coordinate frame co-moving with helical motion: $\widetilde{\mathbf{r}} = \mathbf{r} - \mathbf{h}(z)$. Doing so, and introducing the phase

$$\psi(\mathbf{r}, z) = \widetilde{\psi}(\widetilde{\mathbf{r}}, z)\exp\left(\frac{i\int_0^z |\mathbf{h}'(\zeta)|^2 d\zeta}{4}\right),$$

yields

$$i\widetilde{\psi}_z + \left[\widetilde{\nabla} + i\mathbf{A}(z)\right]^2\widetilde{\psi} - V(\widetilde{\mathbf{r}})\widetilde{\psi} + \sigma\left|\widetilde{\psi}\right|^2\widetilde{\psi} = 0, \tag{9.2}$$

where $\widetilde{\nabla} \equiv \partial_{\tilde{x}}\hat{\mathbf{i}} + \partial_{\tilde{y}}\hat{\mathbf{j}}$ yields the vector potential

$$\mathbf{A}(z) = -\frac{\mathbf{h}'(z)}{2}$$

A typical driving function taken is

$$\mathbf{A}(z) = \kappa\left(\sin(\Lambda z + \chi), -\cos(\Lambda z + \chi)\right). \tag{9.3}$$

where κ is the relevant helix radius, $\Lambda = 2\pi/T$ is the angular frequency, and χ is an arbitrary phase shift. There are a few things to note: (a) In the helical frame of reference, the potential $V(\widetilde{\mathbf{r}})$ is stationary. The form of the potential resembles that of Eq. (6.2) for a honeycomb lattice. (b) The coordinate transformation has introduced a magnetic vector potential $\mathbf{A}(z)$. A common feature among Chern insulators is the presence of a magnetic-type field. Opposed to other systems, which use actual magnetic fields [36, 51], here an effective or pseudo magnetic field is generated by the helically-varying waveguide. (c) The helical driving of the system breaks time reversal symmetry (conjugation + $z \to -z$) since $\mathbf{A}(-z) \neq \mathbf{A}(z)$.

Finally, to simplify the problem, the Peierls phase transformation [94,95]

$$\widetilde{\psi}(\widetilde{\mathbf{r}}, z) = \varphi(\widetilde{\mathbf{r}}, z)e^{-i\widetilde{\mathbf{r}}\cdot\mathbf{A}(z)},$$

is applied and reduces Eq. (9.2) to

$$i\varphi_z + \nabla^2\varphi + \mathbf{r}\cdot\mathbf{A}'(z)\varphi - V(\mathbf{r})\varphi + \sigma|\varphi|^2\varphi = 0, \tag{9.4}$$

where the tilde notation has been dropped. This is the final form of the PDE, from which the tight-binding model discussed below is derived.

Next, the field ϕ is expanded in terms of an orbital basis. For this system, a direct Wannier expansion is ineffective since a nonzero Chern number eliminates their exponential decay [56]; however other *indirect* Wannier approaches may be possible [96]. To generate a convenient and analytical basis, we examine the weakly driven and linear limit of Eq. (9.4) where $|\mathbf{A}'(z)| \ll 1$. Physically, a rapidly varying regime where weakly driven regime where $\Lambda \gg 1$ was employed; see [40,41]. Indeed the experiments [37] were in this rapidly varying helical regime. Using these assumptions eliminates all z-dependent coefficients in Eq. (9.4). Note, however, that the variable $\mathbf{r}$ here is in the helical frame of reference, so these orbitals are localized at the oscillating lattice sites (in the original frame of reference).

For a lattice with two sites per unit cell, we look for solutions of the form

$$\varphi(\mathbf{r}, z) = \sum_{m,n}\left[\widetilde{a}_{mn}(z)\phi_{A,mn}(\mathbf{r}) + \widetilde{b}_{mn}(z)\phi_{B,mn}(\mathbf{r})\right]e^{-iEz}, \tag{9.5}$$

where $\phi_{j,mn}(\mathbf{r})$ are orbital functions. In general, the number of distinct orbital terms in the expansion matches the number of lattice sites per unit cell e.g. a lattice with three lattice sites per until cell will have an extra term of the form $\widetilde{c}_{mn}(z)\phi_{C,mn}(\mathbf{r})$. In particular, for the honeycomb lattice the orbital functions are defined by $\phi_{A,mn}(\mathbf{r}) = \phi(\mathbf{r} - m\mathbf{v}_1 - n\mathbf{v}_2 - \mathbf{d}_1)$ and $\phi_{B,mn}(\mathbf{r}) = \phi(\mathbf{r} - m\mathbf{v}_1 - n\mathbf{v}_2)$, where $\phi(\mathbf{r})$ satisfies the orbital equations in (6.3).

From here, the derivation of a tight-binding model follows similar to that of Sections 4 and 6. A set of semi-discrete equations are derived by substituting expansion (9.5) into Eq. (9.4), multiplying by each orbital type, and then integrating over $\mathbb{R}^2$. For typical experimental systems, the potential is deep or has large magnitude at the waveguides, that is $|V(\mathbf{r})| \gg 1$ near the lattice sites. As a result, a tight-binding approximation is applied

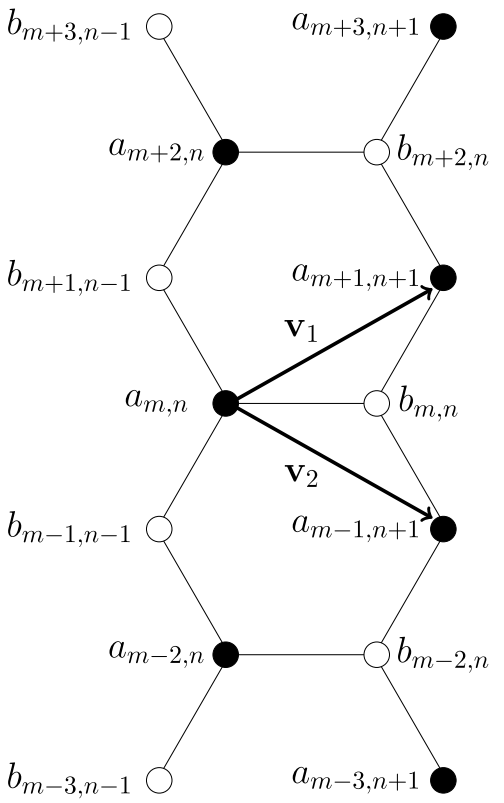

Fig. 19. Discrete honeycomb lattice for the tight-binding system (9.6)–(9.7). The a lattices sites (black dots) are located at points $\{\mathbf{v}_a | \mathbf{v}_a = m\mathbf{w}_1 + n\mathbf{w}_2 + \mathbf{d}_1\}$ and the b sites (white dots) at $\{\mathbf{v}_b | \mathbf{v}_b = m\mathbf{w}_1 + n\mathbf{w}_2\}$ where $m, n \in \mathbb{Z}$. Zig-zag boundary conditions are those in the vertical direction.

and only the on-site and nearest neighbor interactions are kept. Details of the derivation can be found in [41,42].

The paradigm Floquet tight-binding model is a honeycomb lattice. Following the procedure described above, the governing tight-binding model is given by

$$i\frac{da_{mn}}{dz} + \sigma g|a_{mn}|^2 a_{mn} + C\left[e^{-i\mathbf{d}_1\cdot\mathbf{A}(z)}b_{mn} + e^{-i\mathbf{d}_3\cdot\mathbf{A}(z)}b_{m-1,n-1} + e^{-i\mathbf{d}_2\cdot\mathbf{A}(z)}b_{m+1,n-1}\right] = 0, \tag{9.6}$$

$$i\frac{db_{mn}}{dz} + \sigma g|b_{mn}|^2 b_{mn} + C\left[e^{i\mathbf{d}_1\cdot\mathbf{A}(z)}a_{mn} + e^{i\mathbf{d}_3\cdot\mathbf{A}(z)}a_{m+1,n+1} + e^{i\mathbf{d}_2\cdot\mathbf{A}(z)}a_{m-1,n+1}\right] = 0, \tag{9.7}$$

where $g = \int \phi_A^4(\mathbf{r})d\mathbf{r} = \int \phi_B^4(\mathbf{r})d\mathbf{r}$. A couple of notes about this system: (a) The above system is essentially the same as the one discussed in Section 6 –see Eq. (6.9)–(6.10) only now the coefficients are periodic functions of z. (b) The coefficient $C = C(\|\mathbf{v}\|)$ is distance-dependent and so it is the same for all nearest neighbor interactions. (c) The indices used here are not in terms of the lattice vectors $\mathbf{v}_1$ and $\mathbf{v}_2$. Instead, the m index is in terms of the vector $\mathbf{w}_1 = (\mathbf{v}_1 - \mathbf{v}_2)/2 = l(0, 1/2)$ and the n-index for $\mathbf{w}_2 = (\mathbf{v}_1 + \mathbf{v}_2)/2 = l(\sqrt{3}/2, 0)$ (see Fig. 19); this is useful in edge mode calculations, discussed below.

9.1. Floquet dispersion bands

To begin analyzing the honeycomb Floquet system, we first consider the linearized version of system (9.6)–(9.7) on an infinite domain. A linear reduction can be achieved by taking a small intensity field: $|a_{mn}|^2, |b_{mn}|^2 \approx 0$. The corresponding eigenmodes

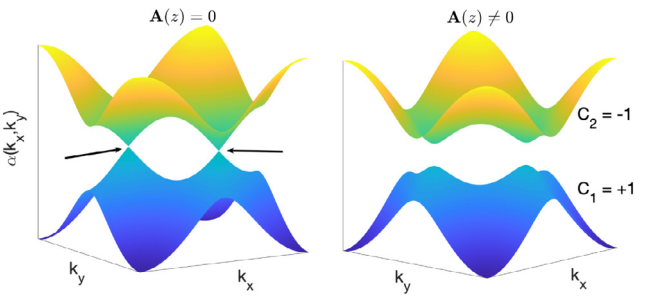

Fig. 20. Typical bulk dispersion surfaces (9.11) computed from (9.9). In the absence of driving ($\mathbf{A}(z) = 0$), the surfaces touch at the Dirac points, K and K'. Driving the lattice ($\mathbf{A}(z) \neq 0$) opens a band gap and the corresponding eigenfunctions acquire nontrivial Chern numbers, as indicated.

are known as bulk modes. The spectral dispersion surfaces or bands are computed by looking for Fourier solutions of the form

$$a_{mn}(z) = A(\mathbf{k}, z)e^{i\mathbf{k}\cdot(m\mathbf{w}_1 + n\mathbf{w}_2)}, \tag{9.8}$$
$$b_{mn}(z) = B(\mathbf{k}, z)e^{i\mathbf{k}\cdot(m\mathbf{w}_1 + n\mathbf{w}_2)},$$

which yield

$$\frac{d\mathbf{c}}{dz} = i\mathcal{H}(\mathbf{k}, z)\mathbf{c}, \qquad \mathbf{c} = \begin{pmatrix} A \\ B \end{pmatrix}(\mathbf{k}, z), \tag{9.9}$$

for (the Hamiltonian)

$$\mathcal{H}(\mathbf{k}, z) = \begin{pmatrix} 0 & \tau(\mathbf{k}, z) \\ \tau(\mathbf{k}, z)^* & 0 \end{pmatrix},$$

and $\tau(\mathbf{k}, z) = e^{-i\mathbf{d}_1\cdot\mathbf{A}(z)} + e^{-i(\mathbf{d}_3\cdot\mathbf{A}(z) + \mathbf{k}\cdot\mathbf{v}_1)} + e^{-i(\mathbf{d}_2\cdot\mathbf{A}(z) + \mathbf{k}\cdot\mathbf{v}_2)}$. Notice that the matrix $\mathcal{H}$ is T-periodic in z and periodic in the spectral plane: $\mathcal{H}(\mathbf{k} + p\mathbf{k}_1, z) = \mathcal{H}(\mathbf{k}, z) = \mathcal{H}(\mathbf{k} + q\mathbf{k}_2, z)$ where $p, q \in \mathbb{Z}$.

We look for solutions of system (9.9) via Floquet theory [59]. These solutions are assumed to satisfy the quasi-periodic boundary condition

$$\mathbf{c}(\mathbf{k}, z + T) = \rho\ \mathbf{c}(\mathbf{k}, z), \qquad \rho(\mathbf{k}) = e^{-i\alpha(\mathbf{k})T}. \tag{9.10}$$

The parameter ρ is known as the characteristic or Floquet multiplier and for stable Floquet modes, it lies on the unit circle. To find it, the 2×2 principal fundamental matrix solution of (9.9) at $z = T$ is computed numerically. This matrix solution is known as monodromy matrix. Moreover, the eigenvalues of the monodromy matrix are the Floquet multipliers in Eq. (9.10). Finally, the so-called Floquet exponents are calculated by

$$\alpha(\mathbf{k}) = \frac{i\log[\rho(\mathbf{k})]}{T}. \tag{9.11}$$

The exponential form of the Floquet multiplier in Eq. (9.10) implies an infinite number of solutions, due to periodicity in $\alpha(\mathbf{k})$; i.e. ρ is unchanged by the shift $\alpha \to \alpha + 2\pi/T$. For all results shown here, we only present the principal branch $\alpha(\mathbf{k}) \in [-\pi/T, \pi/T.]$

For a typical set of values, the bulk dispersion surfaces are shown in Fig. 20. In the absence of driving ($\mathbf{A}(z) = 0$), the bands touch at the Dirac points (6.6). Introduction of the helical driving motion ($\mathbf{A}(z) \neq 0$) opens a band gap. Furthermore, as a result of this driving, the corresponding bulk eigenmodes acquire a nontrivial topological number, discussed next.

Through the periodic driving of a waveguide array, it is possible to realize eigenmodes with a nontrivial topological invariant, known as the Chern number. The relevant topological Chern number of eigenfunction $\mathbf{c}_p$ in Eq. (9.1), corresponding to the pth spectral band, is given by

$$C_p = \frac{1}{2\pi i}\iint_{\text{UC}}\left(\frac{\partial\mathbf{c}_p^\dagger}{\partial k_x}\frac{\partial\mathbf{c}_p}{\partial k_y} - \frac{\partial\mathbf{c}_p^\dagger}{\partial k_y}\frac{\partial\mathbf{c}_p}{\partial k_x}\right)d\mathbf{k}, \quad p = 1, 2 \tag{9.12}$$

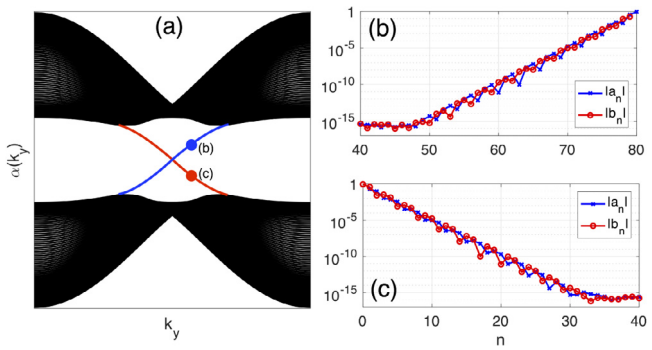

Fig. 21. (a) Linear edge dispersion bands given in Eq. (9.18). The red (blue) gapless bands correspond to edge modes localized along the left (right) domain wall. Black regions correspond to bulk modes. Two typical edge modes are shown in panels (b) and (c) on a semi-log plot to highlight their exponential decay.

where UC denotes the reciprocal unit cell defined in terms of the reciprocal lattice vectors $\mathbf{k}_1$ and $\mathbf{k}_2$. We note that C_p is z-invariant. Physically, the Chern number indicates the presence of a nontrivial phase jump inside the reciprocal unit cell. In a rapidly-varying regime ($T \ll 1$), it is also possible to derive an averaged version of the bulk system (9.1) that is independent of z [97]. Remarkably, it turns out that the form of this the averaged-system is analogous to the well-known Haldane model used to study the quantum Hall effect [34]. On the other hand, to numerically compute Chern numbers directly, the algorithm given in [98] can be applied.

As a remark, nonlinearity can induce localized bulk modes. These nonlinear Floquet modes, predicted in [99] and experimentally observed in [100], correspond to band gap spectral values and exhibit a cyclotronic motion about a particular lattice site.

Next, we study the problem on a finite domain in the x direction and infinite in the y direction. We look for edge modes that decay exponentially fast perpendicular to the imposed boundary. As a result, we consider modes of the form

$$a_{mn}(z) = a_n(\mathbf{k}, z)e^{i\mathbf{k}\cdot m\mathbf{w}_1}, \quad b_{mn}(z) = b_n(\mathbf{k}, z)e^{i\mathbf{k}\cdot m\mathbf{w}_1}, \tag{9.13}$$

which reduce system (9.6)–(9.7) to

$$i\frac{da_n}{dz} + \sigma g|a_n|^2 a_n \tag{9.14}$$
$$+ C\left[e^{-i\mathbf{d}_1\cdot\mathbf{A}(z)}b_n + \left(e^{-i[\mathbf{d}_3\cdot\mathbf{A}(z)+\mathbf{k}\cdot\mathbf{w}_1]} + e^{-i[\mathbf{d}_2\cdot\mathbf{A}(z)-\mathbf{k}\cdot\mathbf{w}_1]}\right) b_{n-1}\right] = 0,$$
$$i\frac{db_n}{dz} + \sigma g|b_n|^2 b_n \tag{9.15}$$
$$+ C\left[e^{i\mathbf{d}_1\cdot\mathbf{A}(z)}a_n + \left(e^{i[\mathbf{d}_3\cdot\mathbf{A}(z)+\mathbf{k}\cdot\mathbf{w}_1]} + e^{i[\mathbf{d}_2\cdot\mathbf{A}(z)-\mathbf{k}\cdot\mathbf{w}_1]}\right) a_{n+1}\right] = 0,$$

where $\mathbf{k}\cdot\mathbf{w}_1 = \frac{l}{2}k_y$. Zero boundary conditions are imposed along a set of zig-zag boundaries:

$$b_n = 0\,, \quad \text{for} \quad n < 0,\ n > N-1, \tag{9.16}$$
$$a_n = 0\,, \quad \text{for} \quad n < 1,\ n > N,$$

(see Fig. 19 for reference).

The linear ($\sigma = 0$) edge Floquet modes can be computed in a manner analogous to that of the bulk problem above. Again, solutions are assumed to satisfy the quasi-periodic boundary condition

$$\begin{pmatrix} a(k_y, z+T) \\ b(k_y, z+T) \end{pmatrix}_n = \rho(k_y)\begin{pmatrix} a(k_y, z) \\ b(k_y, z) \end{pmatrix}_n, \qquad \rho(k_y) = e^{-i\alpha(k_y)T}. \tag{9.17}$$

For the boundary value problem defined in Eqs. (9.14)–(9.16), the corresponding monodromy matrix can be numerically computed at $z = T$ using identity initial conditions. As before, the Floquet exponents are computed from the Floquet multipliers using

$$\alpha(k_y) = \frac{i\log[\rho(k_y)]}{T}, \tag{9.18}$$

and keeping only the fundamental branch.

For a typical driving function $\mathbf{A}(z)$, the Floquet band diagram (corresponding to zero boundary conditions) is shown in Fig. 21(a) using $N = 80$ sites. The black region corresponds to bulk modes whose corresponding eigenmodes do not decay in n. Spanning the bandgap is a chiral edge state, indicated by a family of Floquet quasienergy values (blue and red curves) whose corresponding eigenmodes are localized along the left and right domain walls. In panels Figs. 21(b) and 21(c) the associated edge Floquet modes in Eq. (9.17) are shown and their exponential decay is highlighted.

To gain an intuitive understanding of the chirality of this system, consider the group velocity corresponding to a gapless mode. Along both curves the slope and therefore group velocity is sign-definite. Modes with negative (positive) slope correspond to negative (positive) group velocity localized along the left (right) boundary. The resulting (positive) chiral mode is the combination of these two edge modes; it propagates counterclockwise, as viewed from the waveguide input, along the domain boundary. This is the topological case with nontrivial Chern number. If the Chern number is zero, usually there does not exist chiral edge modes. But there are counterexamples; e.g. phase offset sublattice driving patterns [82].

Topologically protected modes are identified through the bulk-edge correspondence. In the topological case, bulk modes whose band diagrams look like Fig. 21(a) have a nontrivial Chern number. There is a known algebraic relationship between bulk Chern number and the number of topologically protected edge states. The upper bulk band has Chern number $C_2 = -1$, which equals the number of topological edge states in the gap above it (zero) minus the number of edge states in the gap below it (one). A similar algebra exists for the lower bulk band.

As a final observation, topologically protected modes can also be created along the boundary of two topologically distinct media (e.g. different Chern numbers) fused together. These so-called *interface modes* behave similar to the edge modes constructed along a domain wall, i.e. Eq. (9.16), in that they propagate unidirectionally along the interface. These types of arrangements can allow more precise steering of the electromagnetic waves. Physically, topologically protected interface modes have been observed in various Chern insulator systems like gyrotropic lattices [50], Floquet photonic lattices [101], and more generally, systems with a sharp transition between the topologically distinct bulk regions [50,84,102].

9.2. Edge mode dynamics

In this section, the dynamics of the edge modes found in the previous section are discussed, with particular focus on the chiral propagation of the topologically protected modes mentioned above. Wide spatial envelopes, localized along the domain boundary, are found to propagate into and around lattice defects, rather than reflecting or disintegrating. When Kerr nonlinearity is relevant, it is possible to realize Floquet edge solitons which also propagate unidirectionally [40–42,103].

To form an analytical description of edge envelopes, consider waveguides that are rapidly rotating such that the angular frequency in Eq. (9.3) is large: $\Lambda \gg 1$. Furthermore, assume a weakly nonlinear regime where $\sigma g = 1/\Lambda$. A multiple scales analysis (see [40,41]) reveals, to leading order, edge states localized along the left boundary of the form

$$a_{mn}(Z) \sim 0\,, \qquad b_{mn}(z) \sim B(y_m, Z)r^n e^{ik_0 y_m}, \tag{9.19}$$

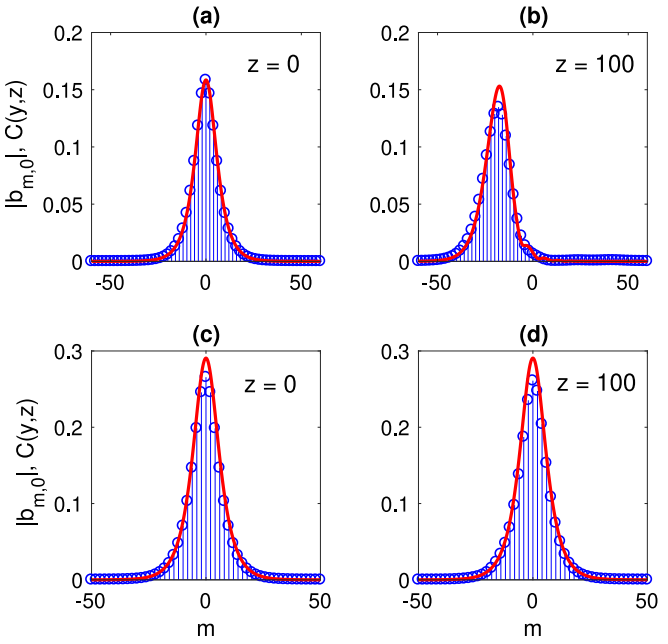

Fig. 22. Profile comparison between the discrete solution (blue circles), $b_{m,0}(z)$, and envelope (red curve), $C(y,z)$. The top row shows an envelope in a parameter regime described by the third-order NLS Eq. (9.24); the bottom row is a stationary bright soliton governed by (9.21). Reprinted figure with permission from [41], copyright (2017) by the American Physical Society.

where Z is a slow time variable, $y_m = \sqrt{3}m/2$ is the continuous variable y sampled at points on the discrete grid, and $|r(k_0)| < 1$ corresponds to an exponentially decaying edge mode as $n \to \infty$. The edge mode excited corresponds to the mode $k_y = k_0$ of the edge band diagram. The slowly-varying envelope $B(y,Z)$ satisfies the generalized NLS equation

$$i\frac{\partial B}{\partial Z} + \alpha_* B + i\alpha_*'\frac{\partial B}{\partial y} + \frac{\alpha_*''}{2}\frac{\partial^2 B}{\partial y^2} - i\frac{\alpha_*'''}{6}\frac{\partial^3 B}{\partial y^3} + \cdots + \alpha_{\rm nl}|B|^2 B + \cdots = 0\,, \tag{9.20}$$

such that $\alpha_{\rm nl} = \|b_n(k_0)\|_4^4 / \left(\Lambda \|b_n(k_0)\|_2^2\right) \geq 0$ and $\alpha_*^{(p)} = \frac{d^p\alpha}{dk_y^p}\big|_{k_y=k_0}$ for the red curve in Fig. 21(a). A similar calculation on the right boundary shows that a_{mn} is the nontrivial contribution while b_{mn} is nearly zero. In the linear regime, the governing equation only contains linear contributions, i.e. $\alpha_{\rm nl} = 0$.

Through the careful selection of physical parameters, it is possible to engineer so-called Floquet edge solitons. A slowly-varying envelope $B(y,Z)$ means that the higher-order dispersion terms (beyond third-order) in Eq. (9.20) are typically negligible. Moreover, at moderate power levels the higher-order nonlinearity terms (beyond cubic Kerr term) can be neglected too. By judiciously picking the wavenumber, k_0, certain linear terms can be effectively eliminated. For example, near a critical point of an edge band (see Fig. 21(a)), $\alpha_*'' \neq 0$ and $\alpha_*''' \approx 0$. As a result, the governing equation of the envelope is the traveling NLS equation

$$i\frac{\partial B}{\partial Z} + \alpha_* B + i\alpha_*'\frac{\partial B}{\partial y} + \frac{\alpha_*''}{2}\frac{\partial^2 B}{\partial y^2} + \alpha_{\rm nl}|B|^2 B = 0, \tag{9.21}$$

for which $\alpha_*'' > 0$ admits the bright soliton solution

$$B(y,Z) = \nu\sqrt{\frac{\alpha_*''}{\alpha_{\rm nl}}}\,{\rm sech}\left[\nu\left(y - \alpha_*' Z\right)\right] e^{i\left(\frac{\alpha_*''\nu^2}{2} + \alpha_*\right)Z}, \tag{9.22}$$

with $\nu \in \mathbb{R}$. Experimentally, Floquet solitons have been observed in the bulk [100] and along the edge [104]. In the case of $\alpha_*'' < 0$,

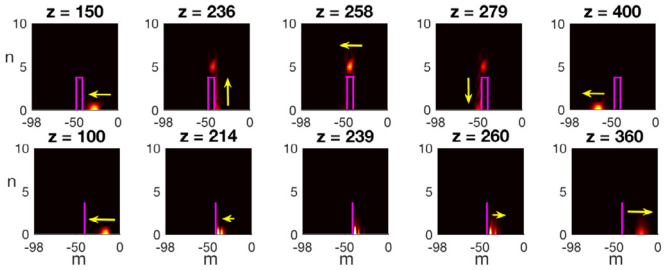

Fig. 23. Intensity snapshots, $|b_{mn}(z)|^2$, for a (top row) topologically protected mode and (bottom row) non-topologically protected mode. The defect barrier is located in the region $[-46,-40] \times [0,4]$. Reprinted figure with permission from [41], copyright (2017) by the American Physical Society.

this equation admits dark solitons of the form

$$B(y,Z) = \nu\sqrt{-\frac{\alpha_*''}{\alpha_{\rm nl}}}\left[\cos\alpha + i\sin\alpha\ \tanh\left(\nu\left[y - \left(\alpha_*' - \nu\alpha_*''\cos\alpha\right)Z\right]\right)\right] e^{i(\alpha_* - \nu^2\alpha_*'')Z}, \tag{9.23}$$

where ν and α are real parameters.

On the other hand, if one considers modal values near the inflection point of Fig. 21(a), then $\alpha_*'' \approx 0$ while $\alpha_*''' \neq 0$ and (9.20) reduces to the third-order NLS equation

$$i\frac{\partial B}{\partial Z} + \alpha_* B + i\alpha_*'\frac{\partial B}{\partial y} - i\frac{\alpha_*'''}{6}\frac{\partial^3 B}{\partial y^3} + \alpha_{\rm nl}|B|^2 B = 0, \tag{9.24}$$

for which no stable solitons are known; in this case there is considerable dispersion. Theoretically, one expects solitons away from the zero dispersion point to propagate more effectively over long distances than modes at the zero dispersion point.

A comparison of the envelope approximation in (9.19) with the full numerical solution of (9.6)–(9.7) is shown in Fig. 22. In the case of the soliton being described by the higher-order NLS Eq. (9.24), the envelope and discrete model both are seen to develop dispersive tails at large z. On the other hand, the stationary bright soliton profile is seen to maintain its form over long distances.

The final consideration is the effect of the topological protection on the edge envelope evolution. A defect barrier is introduced along the boundary wall. Physically, this defect corresponds to an absence of waveguides, so $a_{mn} = 0$ and $b_{mn} = 0$ is imposed in that region. The evolution of a linear edge envelope with an associated nontrivial Chern number is displayed in the top row of Fig. 23. The envelope encounters the defect barrier, and rather than backscatter, propagates around and with virtually no loss in intensity. On the other hand, if one considers a non-topological edge envelope, the contrast is stark (see bottom row of Fig. 23). The envelope propagates into the barrier, reflects backward and loses a substantial amount of energy.

A similar evolution follows for the edge solitons described above (see [41]). A potential advantage of incorporating nonlinearity is the reduction or removal of dispersion in envelopes. As was seen in Fig. 22, dispersive degradation of modes is possible over long distances. In theory, a soliton is a perfect balance of dispersive broadening and self-focusing nonlinearity. Floquet edge solitons have the potential to combine the robust unidirectional propagation of topological edge modes with a stable soliton balance.

Finally, we remark on the case of narrow (in y) envelopes for this system. In the absence of driving ($\mathbf{A}(z) = 0$), generally traveling solitary waves are not supported by the discrete NLS

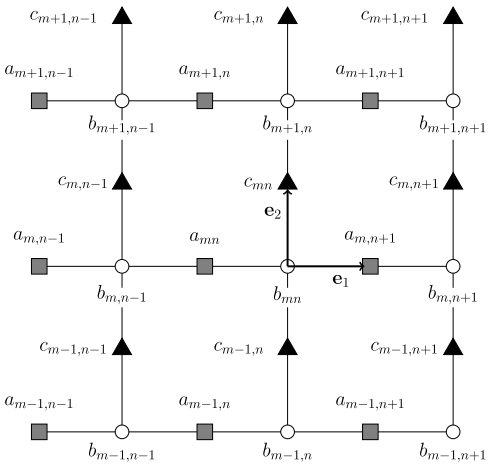

Fig. 24. The Lieb lattice consists of three interpenetrating square sublattices $V_a(\mathbf{r})$ (square site, **a**), $V_b(\mathbf{r})$ (circle site, **b**) and $V_c(\mathbf{r})$ (triangle site, **c**). The lattice vectors are $\mathbf{e}_1 = (l, 0)$ and $\mathbf{e}_2 = (0, l)$. Lines denote nearest neighbor interactions. Shown is a bearded (straight) boundary condition on the left (right) edge. Reprinted figure with permission from [42], copyright (2019) by the American Physical Society.

equation [105,106]. This effect is due to discretization of the original PDE, and is commonly known as the Peierls–Nabarro energy barrier [107]. Recently, it was shown that the topological nature of these systems does not allow highly localized modes to stop [108], i.e. traveling modes exist. However, the solitary wave sheds energy until it widens its profile and is effectively continuous and described by the envelope in Eq. (9.22). The need to carefully prepare nonlinear edge states was also observed in [50], albeit in a physically different system. In that latter work, solutions of the linear system were found to suffer from decoherence in the fully nonlinear system. Care must me taken when preparing coherent nonlinear modes.

9.3. Other lattice models

Longitudinally-driven lattice models can be constructed for other lattice types and with them their own unique band diagrams. Examples include staggered-square [41,109], Lieb [110], and kagome lattices [42,111]. Each case allows topologically protected, unidirectional edge mode propagation. The principles used to derive a set of governing tight-binding models are similar to those used to obtain the honeycomb lattice above.

An interesting example is the Lieb Floquet lattice (see Fig. 24) which contains three lattice sites per unit cell. The central (b)-site couples to the four nearest neighbor sites: two (a)-sites and two (c)-sites. The (a) and (c) sites do not directly couple to each other, that is a next-nearest neighbor interaction. The governing tight-binding model is given by the system of three equations

$$i\frac{da_{mn}}{dz} + C\left[e^{i\mathbf{e}_1\cdot\mathbf{A}(z)}b_{mn} + e^{-i\mathbf{e}_1\cdot\mathbf{A}(z)}b_{m,n-1}\right] + \sigma g|a_{mn}|^2 a_{mn} = 0, \tag{9.25}$$

$$i\frac{db_{mn}}{dz} + C\left[e^{i\mathbf{e}_1\cdot\mathbf{A}(z)}a_{m,n+1} + e^{-i\mathbf{e}_1\cdot\mathbf{A}(z)}a_{mn} + e^{i\mathbf{e}_2\cdot\mathbf{A}(z)}c_{mn} + e^{-i\mathbf{e}_2\cdot\mathbf{A}(z)}c_{m-1,n}\right] + \sigma g|b_{mn}|^2 b_{mn} = 0, \tag{9.26}$$

$$i\frac{dc_{mn}}{dz} + C\left[e^{i\mathbf{e}_2\cdot\mathbf{A}(z)}b_{m+1,n} + e^{-i\mathbf{e}_2\cdot\mathbf{A}(z)}b_{mn}\right] + \sigma g|c_{mn}|^2 c_{mn} = 0, \tag{9.27}$$

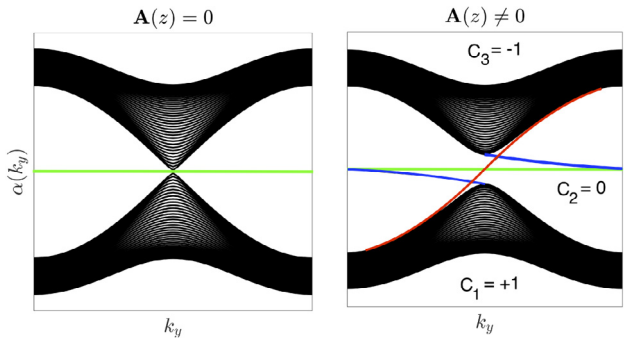

Fig. 25. Lieb lattice edge band diagrams for bearded (straight) boundary conditions on the left (right) boundary. Red curves indicate edge modes on the right edge, blue curves denote left edge modes, and green curves designate flat band modes on both edges. When driven, the Chern numbers for the corresponding bulk bands are shown.

such that $g = \int \phi_A^4(\mathbf{r})d\mathbf{r} = \int \phi_B^4(\mathbf{r})d\mathbf{r} = \int \phi_C^4(\mathbf{r})d\mathbf{r}$.

The corresponding bulk and edge dispersion bands can be computed in manner similar to the honeycomb lattice in Section 9.1. In the absence of driving, the bulk dispersion surfaces are characterized by the single Dirac point in the reciprocal unit cell where all three bands meet [97]. The top and bottom bands exhibit locally conical structure near the Dirac point while the middle band is completely flat. Helically driving the waveguide opens a band gap between the top, bottom, and (flat) middle bands. The eigenmodes of the top and bottom bulk bands can acquire nontrivial Chern numbers.

A typical edge band diagram for the Lieb lattice is shown in Fig. 25. Driving the lattice opens two gaps: between the top and middle bands and between the bottom and middle. Within each gap is a single chiral edge state that spans the gap. As a result, the central band has a Chern number of zero ($1 - 1 = 0$). Moreover, flat band edge modes are stationary and do not suffer from dispersion/diffractive effects [112,113]. Similar to the honeycomb lattice, the gapless edge modes propagate unidirectionally around lattice defects, scatter-free (see [42] for details). Edge solitons have been predicted for the Lieb lattice in [114], meanwhile dipole solitons have been theorized in the kagome lattice [115].

10. Conclusions

Photonic waveguide arrays are a versatile platform for realizing interesting physical phenomena. This article discusses some of the important experimental and theoretical work in the field. The field of optical waveguides is vast; the focus of this article was primarily on work done in the last decade.

The history of early experiments and their mathematical models was reviewed. Most experimentally realizable parameter regimes correspond to strong waveguide attraction which are effectively modeled by deep lattice potentials. As a result, the derivation of and study of various tight-binding models is a useful consideration. Here, tight-binding models in one and two spatial dimensions were examined. Emphasis was placed on the orbital expansion technique due to its ability to yield analytical descriptions of coupling coefficients. Numerous physical phenomena are found, including: Dirac cones, conical diffraction, gap solitons, topologically protected modes, and Floquet linear edge mode and nonlinear edge solitons.

Importantly, photonic waveguide arrays can be experimentally realized. Such waveguides are usually constructed in the paraxial regime and are governed by the Schrödinger equation with a periodic potential. The interesting phenomena discussed in this paper makes it likely that the study of photonic waveguide

arrays and associated topological waves will continue to draw considerable research interest in physics, engineering and applied mathematics for many years.

Declaration of competing interest

The authors declare that they have no known competing financial interests or personal relationships that could have appeared to influence the work reported in this paper.

Acknowledgments

This work was partially supported by AFOSR, USA under Grant No. FA9550-19-1-0084 and National Science Foundation, USA under Grant DMS-2005343.

References

[1] D.N. Christodoulides, R.I. Joseph, Discrete self-focusing in nonlinear arrays of coupled waveguides, Opt. Lett. 13 (9) (1998) 794–796.
[2] P.G. Kevrekidis, K.O. Rasmussen, A.R. Bishop, The discrete nonlinear Schrödinger equation: a survey of recent results, Internat. J. Modern Phys. B 15 (2001) 2833–2900.
[3] M.J. Ablowitz, Z. Musslimani, Discrete spatial solitions in a diffraction-managed nonlinear waveguide array: a unified approach, Physica D 184 (2003) 276–303.
[4] H.S. Eisenberg, Y. Silberberg, R. Morandotti, A.R. Boyd, J.S. Aitchison, Discrete spatial optical solitons in waveguide arrays, Phys. Rev. Lett. 81 (1998).
[5] N.K. Efremidis, S. Sears, D.N. Christodoulides, J. Fleischer, M. Segev, Discrete solitons in photorefractive optically induced photonic lattices, Phys. Rev. E 66 (2002) 046602.
[6] J.W. Fleischer, T. Carmon, M. Segev, N. Efremidis, D.N. Christodoulides, Observation of discrete solitons in optically induced real time waveguide arrays, Phys. Rev. Lett. 90 (2003) 023902.
[7] J.W. Fleischer, M. Segev, N.K. Efremidis, D.N. Christodoulides, Observation of two-dimensional discrete solitons in optically induced nonlinear photonic lattices, Nature 422 (2003) 147–150.
[8] J.K. Yang, I. Makasyuk, A. Bezryadina, Z. Chen, Dipole solitons in optically induced two-dimensional photonic lattices, Opt. Lett. 29 (2004) 1662–1664.
[9] D.N. Neshev, T.J. Alexander, E.A. Ostrovskaya, Y.S. Kivshar, H. Martin, I. Makasyuk, Z.G. Chen, Observation of discrete vortex solitons in optically induced photonic lattices, Phys. Rev. Lett. 92 (2004) 123903.
[10] X. Wang, Z. Chen, J. Wang, J.K. Yang, Observation of in-band lattice solitons, Phys. Rev. Lett. 99 (2007) 243901.
[11] C.J. Pethick, H. Smith, Bose-Einstein Condensation in Dilute Gase, Cambridge University Press, 2008.
[12] N.K. Efremidis, J. Hudock, D. D. N. Christodoulides, J.W. Fleischer, O. Cohen, M. Segev, Two-dimenional optical lattice solitons, Phys. Rev. Lett. 91 (2003) 213906.
[13] R. Fischer, D. Trager, D.N. Neshev, A.A. Sukhorukov, W. Krolikowski, C. Denz, Y.S. Kivshar, Reduced-symmetry two-dimensional solitons in photonic lattices, Phys. Rev. Lett. 96 (2006) 023905.
[14] D. Trager, R. Fischer, D.N. Neshev, A.A. Sukhorukov, C. Denz, W. Krolikowski, Y.S. Kivshar, Nonlinear Bloch modes in two-dimensional photonic lattices, Opt. Express 14 (2006) 1913–1923.
[15] O. Morsch, M. Oberthaler, Dynamics of Bose-Einstein condensates in optical lattices, Rev. Modern Phys. 1 (2006) 179–215.
[16] E.A. Ostrovskaya, Y.S. Kivshar, Matter-wave gap vortices in optical lattices, Phys. Rev. Lett. 93 (2004) 160405.
[17] F. Odeh, J.B. Keller, Partial differential equations with periodic coefficients and Bloch waves in crystals, J. Math. Phys. 5 (1964) 1499–1503.
[18] M.J. Ablowitz, S.D. Nixon, Y. Zhu, Conical diffraction in honeycomb lattices, Phys. Rev. A 79 (2009) 053830.
[19] O. Manela, G. Bartal, M. Segev, H. Buljan, Spatial supercontinuum generation in nonlinear photonic lattices, Opt. Lett. 31 (2006) 2320–2322.
[20] R. Dong, C.E. Ruter, D. Kip, O. Manela, M. Segev, C.L. Yang, J.J. Xu, Spatial frequency combs and supercontinuum generation in one-dimensional photonic lattices, Phys. Rev. Lett. 101 (2008) 183903.
[21] T. Dohnal, D. Pelinovsky, G. Schneider, Coupled-mode equations and gap solitons in a two-dimensional nonlinear elliptic problem with a separable periodic potential, J. Nonlinear Sci. 19 (2009) 95–131.
[22] T. Dohnal, H. Uecker, Coupled mode equations and gap solitons for the 2D Gross–Pitaevskii equation with a non-separable periodic potential, Physica D 238 (2009) 860–879.
[23] B. Ilan, M.I. Weinstein, Band-edge solitons, nonlinear Schrödinger/Gross–Pitaevskii equations, and effective media, Multiscale Model. Simul. 8 (2010) 1055–1101.
[24] D. Pelinovsky, Localization in Periodic Potentials: from Schrodinger Operators to the Gross-Pitaevskii Equation, Vol. 390, Cambridge University Press, 2011.
[25] G.L. Alfimov, P.G. Kevrekidis, V.V. Konotop, M. Salerno, Wannier functions analysis of the nonlinear Schrödinger equation with a periodic potential, Phys. Rev. E 66 (2002) 046608.
[26] C.L. Fefferman, M.I. Weinstein, Honeycomb lattice potentials and Dirac points, J. Am. Math. Soc. 25 (2012) 1169–1220.
[27] O. Peleg, G. Bartal, B. Freedman, O. Manela, M. Segev, D.N. Christodoulides, Conical diffraction and gap solitons in honeycomb photonic lattices, Phys. Rev. Lett. 98 (2007) 103901.
[28] M.V. Berry, M.R. Jeffrey, Conical diffraction: Hamilton's diabolical point at the heart of crystal optics, Prog. Opt. 50 (2007) 13–50.
[29] P.G. Kevrekidis, B.A. Malomed, Y.B. Gaididei, Solitons in triangular and honeycomb dynamical lattices with the cubic nonlinearity, Phys. Rev. E 66 (2002) 016609.
[30] A.K. Geim, K.S. Novoselov, The rise of graphene, Nature Mater. 6 (2007) 183–191.
[31] L.H. Haddad, L.C. Carr, The nonlinear Dirac equation in Bose-Einstein condensates: foundation and symmetries, Physica D 238 (2009) 1413–1421.
[32] K. v. Klitzing, G. Dorda, M. Pepper, New method for high-accuracy determination of the fine-structure constant based on quantized hall resistance, Phys. Rev. Lett. 45 (1980) 494.
[33] D.J. Thouless, M. Kohmoto, M.P. Nightingale, M. den Nijs, Quantized hall conductance in a two-dimensional periodic potential, Phys. Rev. Lett. 49 (1982) 405.
[34] F.D.M. Haldane, Model for a quantum hall effect without Landau levels: condensed-matter realization of the "parity anomaly", Phys. Rev. Lett. 61 (1988) 2015.
[35] F.D.M. Haldane, S. Raghu, Possible realization of directional optical waveguides in photonic crystals with broken time-reversal symmetry, Phys. Rev. Lett. 100 (2008) 013904.
[36] Z. Wang, Y. Chong, J.D. Joannopoulos, M. Soljačić, Observation of unidirectional backscattering-immune topological electromagnetic states, Nature 461 (2009) 772.
[37] M.C. Rechtsman, J.M. Zeuner, Y. Plotnik, Y. Lumer, D. Podolsky, F. Dreisow, S. Nolte, M. Segev, A. Szameit, Photonic floquet topological insulators, Nature 496 (2013) 196.
[38] L. Lu, J.D. Joannopoulos, M. Soljačić, Topological photonics, Nat. Photonics 8 (2014) 821.
[39] T. Ozawa, H.M. Price, A. Amo, N. Goldman, M. Hafezi, L. Lu, M.C. Rechtsman, D. Schuster, J. Simon, O. Zilberberg, I. Carusotto, Topological photonics, Rev. Modern Phys. 91 (2019) 015006.
[40] M. Ablowitz, C. Curtis, Y.-P. Ma, Linear and nonlinear traveling edge waves in optical honeycomb lattices, Phys. Rev. A 90 (2014) 023813.
[41] M.J. Ablowitz, J.T. Cole, Tight-binding methods for general longitudinally driven photonic lattices: Edge states and solitons, Phys. Rev. A 96 (2017) 043868.
[42] M.J. Ablowitz, J.T. Cole, Topological insulators in longitudinally driven waveguides: Lieb and kagome lattices, Phys. Rev. A 99 (2019) 033821.
[43] K.G. Makris, R. El-Ganainy, D.N. Christodoulides, Z.H. Musslimani, Beam dynamics in PT symmetric optical lattices, Phys. Rev. Lett. 100 (2008) 103904.
[44] Z.H. Musslimani, K.G. Makris, R. El-Ganainy, D.N. Christodoulides, Optical solitons in PT periodic potentials, Phys. Rev. Lett. 100 (2008) 030402.
[45] C.E. Rüter, K.G. Makris, R. El-Ganainy, D.N. Christodoulides, M. Segev, D. Kip, Observation of parity–time symmetry in optics, Nat. Phys. 6 (2010) 192–195.
[46] A. Guo, G.J. Salamo, D. Duchesne, R. Morandotti, M. Volatier-Ravat, V. Aimez, G.A. Siviloglou, D.N. Christodoulides, Observation of PT-symmetry breaking in complex optical potentials, Phys. Rev. Lett. 103 (2009) 093902.
[47] J.P. Lee-Thorp, M.I. Weinstein, Y. Zhu, Elliptic operators with honeycomb symmetry: Dirac points, edge states and applications to photonic graphene, Arch. Ration. Mech. Anal. 232 (2019) 1–63.
[48] M. Cassier, M.I. Weinstein, High contrast elliptic operators in honeycomb structures, Multiscale Model. Simul. 19 (2021) 1784–1856.
[49] H. Ammari, B. Fitzpatrick, E.O. Hiltunen, H. Lee, S. Yu, Honeycomb-lattice minnaert bubbles, SIAM J. Math. Anal. 52 (2020) 5441–5466.
[50] P. Hu, L. Hong, Y. Zhu, Linear and nonlinear electromagnetic waves in modulated honeycomb media, Stud. Appl. Math. 144 (2020) 18–45.
[51] Z. Wang, Y.D. Chong, J.D. Joannopoulos, M. Soljačić, Reflection-free one-way edge modes in a gyromagnetic photonic crystal, Phys. Rev. Lett. 100 (2008) 013905.
[52] M. Ablowitz, Y. Zhu, Evolution of Bloch-mode-envelopes in two-dimensional generalized honeycomb lattices, Phys. Rev. A 82 (2010) 013840.

[53] M.J. Ablowitz, Y. Zhu, Unified orbital description of the envelope dynamics in two-dimensional simple periodic lattices, Stud. Appl. Math. 131 (2013) 41–71.
[54] R. Boyd, Nonlinear Optics, Academic Press, 2008.
[55] J. Yang, Nonlinear Waves in Integrable and Nonintegrable Systems, SIAM, 2010.
[56] C. Brouder, G. Panati, M. Calandra, C. Mourougane, N. Marzari, Exponential localization of wannier functions in insulators, Phys. Rev. Lett. 98 (2007) 046402.
[57] G. Wannier, The structure of electronic excitation levels in insulating crystals, Phys. Rev. 52 (1937) 191–197.
[58] J. Callaway, Quantum Theory of the Solid State, Academic Press, 1991.
[59] M. Eastham, The Spectral Theory of Periodic Differential Equations, Scottish Academic Press, Edinburgh, 1973.
[60] P. Kuchment, Floquet Theory for Partial Differential Equations, Birkhauser Verlag, Basel, 1993.
[61] M.J. Ablowitz, C.W. Curtis, Y. Zhu, On tight-binding approximations in optical lattices, Stud. Appl. Math. 129 (2012) 362–388.
[62] C.L. Fefferman, J.P. Lee-Thorp, M.I. Weinstein, Honeycomb Schrödinger operators in the strong binding regime, Comm. Pure Appl. Math. 71 (2018) 1178–1270.
[63] D. Pelinovsky, G. Schneider, Bounds on the tight-binding approximation for the gross–pitaevskii equation with a periodic potential, J. Differential Equations 248 (2010) 837–849.
[64] D. Pelinovsky, G. Schneider, R.S. MacKay, Justification of the lattice equation for a nonlinear elliptic problem with a periodic potential, Comm. Math. Phys. 284 (2008) 803–831.
[65] Z. Shi, J.K. Yang, Solitary waves bifurcated from Bloch-band edges in two-dimesional periodic media, Phys. Rev. E 75 (2007) 056602.
[66] M.J. Ablowitz, H. Segur, Solitons and the Inverse Scattering Transform, SIAM, 1981.
[67] D. Griffiths, Introduction to Quantum Mechanics, Prectice-Hall, 2004.
[68] M.V. Berry, M.R. Jeffrey, J.G. Lunney, Conical diffraction: observations and theory, Proc. R. Soc. Lond. Ser. A Math. Phys. Eng. Sci. 462 (2006) 1629.
[69] P. Wallace, The band theory of graphite, Phys. Rev. 71 (1947).
[70] K.S. Novoselov, A.K. Geim, S.V. Morozov, D. Jiang, Y. Zhang, S.V. Dubonos, I.V. Grigorieva, A.A. Firsov, Electric field effect in atomically thin carbon films, Science 306 (2004) 666–669.
[71] W. Hamilton, Third supplement to an essay on the theory of systems of rays, Trans. R. Irish Acad. 17 (1837) 1.
[72] H. Lloyd, On the phenomena presented by light in its passage along the axes of biaxial crystals, Trans. R. Irish Acad. 17 (1837) 145.
[73] O. Bahat-Treidel, O. Peleg, M. Segev, Symmetry breaking in honeycomb photonic lattices, Opt. Lett. 33 (2008) 2251–2253.
[74] M.J. Ablowitz, Y. Zhu, Nonlinear diffraction in photonic graphene, Opt. Lett. 36 (2011) 3762–3764.
[75] M.J. Ablowitz, Y. Zhu, Nonlinear wave packets in deformed honeycomb lattices, SIAM J. Appl. Math. 87 (2013) 1959–1979.
[76] M. Ablowitz, Y. Zhu, Nonlinear waves in shallow honeycomb lattices, SIAM J. Appl. Math. 72 (2012) 240–260.
[77] C.L. Fefferman, J.P. Lee-Thorp, M.I. Weinstein, Edge states in honeycomb structures, Ann. PDE 2 (2016) 12.
[78] W.P. Su, J.R. Schrieffer, A.J. Heeger, Solitons in polyacetylene, Phys. Rev. Lett. 42 (25) (1979) 1698–1701.
[79] J. Zak, Berry's phase for energy bands in solids, Phys. Rev. Lett. 62 (1989) 2747–2750.
[80] M. Berry, Quantal phase factors accompanying adiabatic changes, Proc. R. Soc. Lond. Ser. A Math. Phys. Eng. Sci. 392 (1984) 45–57.
[81] J.K. Asbóth, L. Oroszlány, A. Pályi, A Short Course on Topological Insulators, in: LNP, vol. 919, Springer, 2016.
[82] M.S. Rudner, N.H. Lindner, E. Berg, M. Levin, Anomalous edge states and the bulk-edge correspondence for periodically driven two-dimensional systems, Phys. Rev. X 3 (2013) 031005.
[83] A. Drouot, The bulk-edge correspondence for continuous honeycomb lattices, Commun. Part. Diff. Eqns. 44 (2019) 1406–1430.
[84] A. Drouot, Microlocal analysis of the bulk-edge correspondence, Comm. Math. Phys. 383 (2021) 2069–2112.
[85] A. Szameit, J. Burghoff, T. Pertsch, S. Nolte, A. Tünnermann, F. Lederer, Two-dimensional soliton in cubic fs laser written waveguide arrays in fused silica, Opt. Express 14 (2006) 6055–6062.
[86] N. Malkova, I. Hromada, X. Wang, G. Bryant, Z. Chen, Transition between tamm-like and shockley-like surface states in optically induced photonic superlattices, Phys. Rev. A 80 (2009) 043806.
[87] R.A. Vicencio, M. Johansson, Discrete gap solitons in waveguide arrays with alternating spacings, Phys. Rev. A 79 (2009) 065801.
[88] D.D. Solnyshkov, O. Bleu, B. Teklu, G. Malpuech, Chirality of topological gap solitons in bosonic dimer chains, Phys. Rev. Lett. 118 (2017) 023901.
[89] T. Tuloup, R.W. Bomantara, C.H. Lee, J. Gong, Nonlinearity induced topological physics in momentum space and real space, Phys. Rev. B 102 (2020) 115411.
[90] D.A. Smirnova, L.A. Smirnov, D. Leykam, Y.S. Kivshar, Topological edge states and gap solitons in the nonlinear Dirac model, Laser Photonics Rev. 13 (2019) 1900223.
[91] Y.-P. Ma, H. Susanto, Topological edge solitons and their stability in a nonlinear su-schrieffer-heeger model, Phys. Rev. E 104 (2021) 054206.
[92] Y. Hadad, A.B. Khanikaev, A. Alù, Self-induced topological transitions and edge states supported by nonlinear staggered potentials, Phys. Rev. B 93 (2016) 155112.
[93] Y. Hadad, J.C. Soric, A.B. Khanikaev, A. Alù, Self-induced topological protection in nonlinear circuit arrays, Nat. Electron. 1 (2018) 178–182.
[94] R. Peierls, Zur theorie des diamagnetismus von leitungselektronen, Z. Phys. 80 (1933) 763–791.
[95] J.M. Luttinger, The effect of a magnetic field on electrons in a periodic potential, Phys. Rev. 84 (1955) 814–817.
[96] M.J. Ablowitz, J.T. Cole, Discrete approximation of topologically protected modes in magneto-optical media, Phys. Rev. A 101 (2020) 023811.
[97] M.J. Ablowitz, J.T. Cole, S.D. Nixon, Unified approach to floquet lattices, topological insulators, and their nonlinear dynamics, 2021, arXiv:2206.05832.
[98] T. Fukui, Y. Hatsugai, H. Suzuki, Chern numbers in discretized brillouin zone: efficient method of computing (spin) hall conductances, J. Phys. Soc. Japan 74 (2005) 1674–1677.
[99] Y. Lumer, Y. Plotnik, M.C. Rechtsman, M. Segev, Self-localized states in photonic topological insulators, Phys. Rev. Lett. 111 (2013) 243905.
[100] S. Mukherjee, M.C. Rechtsman, Observation of floquet solitons in a topological bandgap, Science 368 (2020) 856–859.
[101] Z. Shi, M. Zuo, H. Li, D. Preece, Y. Zhang, Z. Chen, Topological edge states and solitons on a dynamically tunable domain wall of two opposing helical waveguide arrays, ACS Photonics 8 (2021) 1077–1084.
[102] G. Bal, S. Becker, A. Drouot, C. Kammerer, J. Lu, A. Watson, Edge state dynamics along curved interfaces, 2021, arXiv:2106.00729.
[103] D. Leykam, Y.D. Chong, Edge solitons in nonlinear-photonic topological insulators, Phys. Rev. Lett. 117 (2016) 143901.
[104] S. Mukherjee, M.C. Rechtsman, Observation of unidirectional solitonlike edge states in nonlinear floquet topological insulators, Phys. Rev. X (2021).
[105] S. Flach, Y. Zolotaryuk, K. Kladko, Moving lattice kinks and pulses: An inverse method, Phys. Rev. E 59 (1999) 6105–6115.
[106] P. Kevrekidis, The discrete nonlinear Schrödinger equation: Mathematical analysis, numerical computations and phys- ical perspectives, in: STMP, (232) Springer, 2009.
[107] M. Jenkinson, M.I. Weinstein, Onsite and offsite bound states of the discrete nonlinear schrodinger equation and the peierls–nabarro barrier, Nonlinearity 29 (2015) 27–86.
[108] M.J. Ablowitz, J.T. Cole, P.-P. Hu., P. Rosenthal, Peierls-nabarro barrier effect in nonlinear floquet topological insulators, Phys. Rev. E 103 (2021) 042214.
[109] L.J. Maczewsky, J.M. Zeuner, S. Nolte, A. Szameit, Observation of photonic anomalous floquet topological insulators, Nature Commun. 8 (2017) 13756.
[110] D. Guzmán-Silva, C. Mejía-Cortés, M.A. Bandres, M.C. Rechtsman, S. Weimann, S. Nolte, M. Segev, A. Szameit, R.A. Vicencio, Experimental observation of bulk and edge transport in photonic Lieb lattices, New J. Phys. 16 (2014) 063061.
[111] Y. Zong, S. Xia, L. Tang, D. Song, Y. Hu, Y. Pei, J. Su, Y. Li, Z. Chen, Observation of localized flat-band states in kagome photonic lattices, Opt. Express 24 (2016) 8877–8885.
[112] S. Mukherjee, A. Spracklen, D. Choudhury, N. Goldman, P. Öhberg, E. Andersson, R.R. Thomson, Observation of a localized flat-band state in a photonic Lieb lattice, Phys. Rev. Lett. 114 (2015) 245504.
[113] R.A. Vicencio, C. Cantillano, L. Morales-Inostroza, B. Real, C. Mejía-Cortés, S. Weimann, A. Szameit, M.I. Molina, Observation of localized states in Lieb photonic lattices, Phys. Rev. Lett. 114 (2015) 245503.
[114] S.K. Ivanov, Y.V. Kartashov, L.J. Maczewsky, A. Szameit, V.V. Konotop, Edge solitons in Lieb topological floquet insulator, Opt. Lett. 45 (2020) 1459–1462.
[115] S.K. Ivanov, Y.V. Kartashov, M. Heinrich, A. Szameit, L. Torner, V.V. Konotop, Topological dipole floquet solitons, Phys. Rev. A 103 (2021) 053507.